A FINITE ELEMENT STUDY OF SLIDING FRICTION BETWEEN ROUGH SURFACES

Thesis

Submitted to

The School of Engineering of the

UNIVERSITY OF DAYTON

In Partial Fulfillment of the Requirements for

The Degree

Master of Science in Civil Engineering

By

Chad Andrew Burton

UNIVERSITY OF DAYTON

Dayton, Ohio

August, 2009

APPROVED BY:

Robert A. Brockman, Ph.D.
Committee Member and Faculty Advisor
Professor, Civil & Environmental
Engineering and Engineering Mechanics

Steven L. Donaldson, Ph.D.
Committee Member
Associate Professor, Civil & Environmental
Engineering and Engineering Mechanics

Anthony N. Palazotto, Ph.D.
Committee Member
Professor
Department of Aeronautics and Astronautics
Air Force Institute of Technology

Malcolm W. Daniels, Ph.D.
Associate Dean
Graduate Engineering Programs & Research
School of Engineering

Joseph E. Saliba, Ph.D.
Dean, School of Engineering

ABSTRACT

A FINITE ELEMENT STUDY OF SLIDING FRICTION BETWEEN ROUGH SURFACES

Name: Chad Andrew Burton
University of Dayton

Advisor: Dr. R. A. Brockman

This study was conducted to determine a frictional coefficient for the event of dry steel on steel sliding which is experienced by the slipper and rail apparatus of the Holloman High Speed Test Track (HHSTT) located at Holloman AFB. Highly detailed surface measurements were conducted on sample pieces from HHSTT and filtered using a low-pass spatial filter in order to simulate varying levels of roughness. These filtered profiles as well as the originals were incorporated into a two-dimensional plane strain finite element model to simulate the surfaces sliding over one another. Reaction forces from the sliding simulations were recorded and compared to determine the friction coefficient. Parameters such as model contact interaction definitions, nominal pressure, and sliding velocity were also altered to determine the effects thereof.

An increase in coefficient of friction was observed with increasing levels of surface roughness, with the highly filtered and therefore least rough profiles

exhibiting friction coefficients independent of surface geometry. Contact interaction definitions had a large effect on the rougher surfaces, and no effect on smoother ones. A decrease in friction was observed with increasing pressure, while small velocity variations produced inconclusive results.

ACKNOWLEDGEMENTS

I would like to express my thanks to Dr. Robert Brockman, whose direction and guidance was vital to the fulfillment of the work herein. His expertise was absolutely invaluable throughout the entire length of this project, and is greatly appreciated.

I would also like to extend a special thanks to Jenny Pierce of the University of Dayton Research Institute, who conducted tests and provided the tools to analyze all the surface profile data evaluated in this paper. Additionally, I would like to thank the Civil Engineering Department for multiple years of support during my time at The University of Dayton.

TABLE OF CONTENTS

LIST OF FIGURES

LIST OF TABLES

LIST OF SYMBOLS

μ = coefficient of friction

S_a = 3-D roughness average

S_q = 3-D root mean square roughness

S_t = asperity peak range

S_{sk} = 3-D profile skewness

S_{ku} = 3-D profile kurtosis

M = number of data points in x direction

N = number of data points in y direction

Z = surface height measured from mean line

Z = surface mean plane

S_p = highest point on surface

S_s = lowest point on surface

R_a = 2-D average roughness

Ω_c = cutoff frequency for profile filter

λ_c = corresponding spatial wavelength to cutoff frequency

σ = flow stress

ε = strain

$\dot{\varepsilon}^*$ = strain rate

T^* = temperature variation

A,B,C,m,n = general coefficients for Johnson-Cook plasticity model

E = elastic modulus

ν = poisson's ratio

ρ = density

c_d = approximate wave speed

L_{min} = shortest element dimension

Δt = element stable time increment

u = nodal variable

p = node location

i = degree of freedom

A_1, A_2 = general coefficients for constraint equation

P = pressure

v = velocity

n = general exponent

μ_0 = friction coefficient in model definition

μ_{eff} = effective or normalized friction coefficient

CHAPTER I

INTRODUCTION

When designing mechanical systems, accounting for the phenomenon of friction, and subsequently wear, is of the utmost importance. Poorly designed parts can lead to premature failure, loss of efficiency, and increased cost due to excessive replacement or maintenance. Therefore, it is of paramount importance that engineers have a good understanding of both friction and wear, and are able to correctly predict the effects thereof.

Of special interest in this paper is a custom built rocket sled employed at the high speed test track facility located at Holloman Air Force Base in New Mexico. The facility is used for a variety of tests that require the unique advantages present only at the base, particularly the ability to reach incredibly high velocities. The exact setup of the sled apparatus changes depending on the nature of each experiment, and is not of interest in this paper. However, the sliding event of the sled is consistent throughout each test and is what will be considered more fully.

The aforementioned rocket sled travels down a fixed rail or set of rails as seen in Figure 1. The sled itself is attached to slippers which are the only part in contact with the rail. These slippers are subjected to continuous and prolonged dry sliding along the rail during testing. The sliding event generates mechanical and thermal

effects on both the rail and slippers, which, in turn, produce significant wear of the rail. Better understanding and modeling of the wear is desired to help reduce the cost of replacing track along with lessening the chance of catastrophic failure during testing.

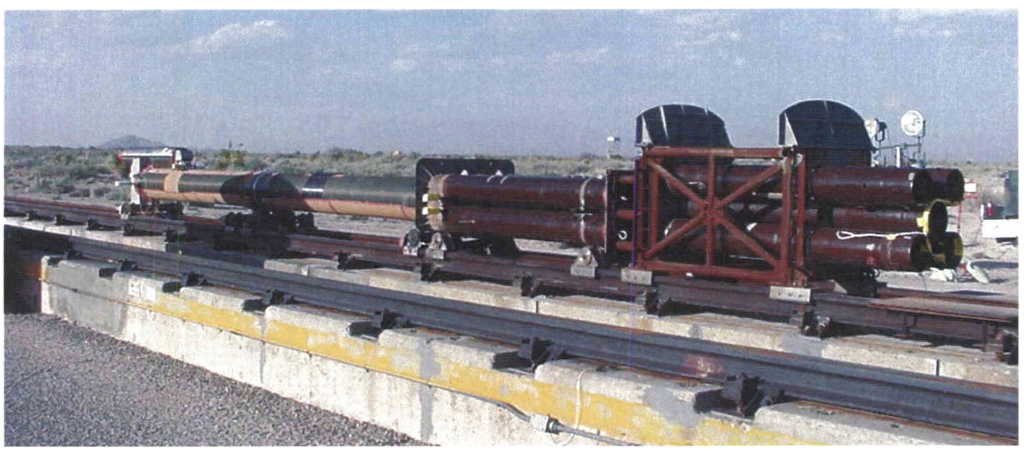

Figure 1: Test sled from 2003

Modeling wear at the velocities attained at the HHSTT present a unique challenge, since the current technologies for controlled wear testing are limited to much lower velocities. Such limitations makes empirical testing like the commonly used pin-on-disk test of limited value due to its inability to correctly account for conditions experienced during actual sled runs. Alternatively, numerical models can be used to attempt to simulate the sliding event observed at HHSTT. However, creating accurate numerical models to simulate wear for the dry sliding event is difficult as well. An accurate prediction of wear requires an accurate model for the

frictional interaction. Such a complex interaction is dependent upon many factors, the most important being: (i) surface finish, (ii) material properties, (iii) sliding velocity, and (iv) weight of the sled. In order to correctly model the friction, these parameters must be taken into account.

While the nature of friction itself is very complicated, the models used to describe them have not been very robust. Until recently, closed-form solutions were the only tool available to most engineers to model frictional behavior. With the proliferation in computing power experienced during the past few decades, finite element analysis has become increasingly useful in many engineering fields, including that of wear modeling. However, their usefulness in wear modeling is still in question due in large part to the overly simplistic friction models they typically employ.

Objective of this Study

The purpose of this paper is to develop an understanding of the relationship between frictional sliding and the parameters applied in describing it using finite element analysis. Physical representations of the surfaces in contact are of special interest and the effects of scale dependence upon frictional force will be determined in order to accurately apply the commonly used friction coefficient at varying levels of detail. Ultimately, the level of detail of the surface model can be reduced to being considered nominally flat while the friction coefficient is correctly accounted for.

Detailed surface profiles will be obtained from provided sample pieces of both slipper and rail and then used to model the solid geometry in the finite element code

ABAQUS. Spatial filtering will then be performed on the surfaces to alter their geometry and determine the effect it has on the model. Subsequent variables, such as pressure and velocity will then be introduced and analyzed to determine their effect on the model as well.

CHAPTER II

REVIEW OF RELATED LITERATURE

Analytical Friction Analysis

Friction has been the subject of great study for centuries. The classical concepts and models of friction are originally provided by Amontons, De Le Hire, Euler, and Coulomb [1]. These models are the first to be able to relate the observed phenomenon of friction into a quantitative relationship which can be used by engineers and scientists. While simplistic, their accuracy and effectiveness have proven themselves over centuries of use. However, the simplicity of the classical models has led to further study into the mechanisms which drive the frictional behavior. Better understanding of these mechanisms can then be used for more sophisticated friction models for today's engineering problems. References [2] through [19] utilize more recent techniques and concepts to describe the nature of friction.

Reference [2] uses experiments on unlubricated metallic surfaces to describe kinetic friction as a series of sticking and slipping interactions caused by the formation and breaking of tiny welds between the surfaces, which is contrary to the classical assumption that frictional sliding is continuous. Also, the earlier developed theory that only surface atoms are affected by frictional sliding is challenged. The experiments uses very low sliding velocities (0.003 - 0.006 cm/s) with various metals

sliding over steel. It is noticed that the choice of material has large effects on the frictional behavior.

In reference [3], Bowden and Tabor use electrical devices to measure conductance across contacting surfaces to illustrate that the real area of contact is far less than the apparent area of contact. This is important, as the definition of real area of contact plays an important role in frictional behavior. The work also demonstrates how the real area of contact increases with load by plastically deforming the tiny asperities which contact each other. Finally, the work demonstrates how, during sliding, the contact area changes drastically and repeatedly, although the average area of contact is close to that of stationary contact.

Using the idea that real area of contact is small compared to nominal area of contact, a number of papers including [4] through[7] attempt to describe the friction by understanding these intimate contacts. Archard shows in [4] that a realistic model for contact includes an increase in both size and number of contact areas with an increase in load, rather than just one or the other. Reference [6] demonstrates that while some plasticity occurs at the asperities during contact, it cannot be entirely plastic as previously thought, but rather some recoverable elastic component must be involved. Greenwood and Williamson [7] are the first to utilize statistical analysis of surface roughness in conjunction with individual asperity contact theories. They provide a means by which to determine if and how much plasticity would occur at individual contacts depending on bulk material properties as well as surface roughness.

Further research using the idea of statistical analysis to relate friction to the surface roughness is completed by Whitehouse [8], Onions [9], Ogilvy [10] [11], and Ford [12]. Whitehouse [8] describes surfaces as a random signal described by a height distribution and an auto correlation function. These parameters are sufficient to describe the surface asperity's peaks, curvature, and distribution. Onions [9] uses the work of [8] to develop a contact theory similar to [7] yet accounting for surface characteristics in a simpler fashion, using a two variable model instead of a three variable model as proposed in [7].

Ogilvy [10] employs the assumption of a Gaussian height distribution, similar to [7], to generate randomly rough surfaces which are then forced into contact with a rigid, smooth half-plane. Both elastic Hertzian and plasticity theory are used to calculate contact parameters, with the elastic analysis tending toward the plastic results as roughness is increased. The adhesive forces at the individual contacts are calculated from the contact parameters to derive the frictional force. Ford [12] combines the works of Greenwood and Williamson [7] with the single asperity model first described by Tabor in [13] to develop a combined adhesion-roughness model for multiple asperity contact. A roughness dependent friction model is then determined with emphasis on the effect of inclination angle between the rough surfaces. The results show less of a contribution to friction coefficient by roughness compared to the single asperity model presented in [13].

Finite Element Friction Modeling

Closed form descriptions of mechanical contact and tangential sliding have been the recipient of much research within the past century as shown above. However, very little has been done in this area using finite element analyses. This can be attributed to a multitude of factors. The combination of the complexity and non-linear nature of contact problems along with lack of commercially available computing power makes accurate analysis very difficult. Only very recently have computers been able to tackle such problems, albeit in a limited way.

The work that has been done using finite elements in friction has been mostly confined to individual asperity modeling, where only single asperities are created and analyzed. While utilizing a consistent approach, the way in which asperities are modeled differ somewhat. In [14], Tangena and Wijnhoven use a two dimensional model of cylindrical asperities, with one asperity being modeled as rigid while the other is modeled as elastic-plastic with isotropic work hardening. The rigid asperity is displaced through the softer asperity at a constant vertical distance or separation. Special attention is given to the effects of this vertical distance as well as asperity radii combinations.

Faulkner and Arnold [15] use a three dimensional finite element model of hemispherical asperities. Their model includes full elastic-plastic behavior with strain hardening for both contacting asperities. At the interface of the asperities both frictionless and Coulomb friction cases are tested. Results from the finite element model are then incorporated into a statistical model which accounts for the presence of multiple asperities being located on an actual surface, and then are compared to

that of Franse et al.[16], which assumed cylindrical asperities. The results show that Faulkner and Arnold's three dimensional model produce friction coefficients lower than that found when using cylindrical asperities. This is due in large part to the allowance of lateral flow of displaced material inherent with hemispherical contact.

Vijaywargiya and Green [17] have also developed a two dimensional model with cylindrical asperities using plane strain assumptions. The asperities in this model are elastic perfectly plastic, which allows a better understanding of the effects of plasticity on the model as a whole and the energy loss caused by it. As in [14] and [15], the asperities are held at a constant vertical position and displaced horizontally over one another. Frictionless cases and interfacial frictional cases are studied and compared. It is observed that material pile-up as well as energy loss due to plasticity is less pronounced for the frictionless case. Also of note was the fact that in frictionless contact the ratio of normal to tangential force is not zero when the asperities are aligned directly above one another.

Torrance, Galligan, and Liraut [18] have studied an asperity model using a hard wedge traversing a softer flat. Attention is given to the inclination angle of the wedge as it represents the roughness of the contacting surface. The angles are kept small (<10 degrees) to simulate surfaces with very smooth surface finishes. Analytical as well as finite element models of the wedge interaction are run with relatively similar results. Discrepancies between the results are noted to be due to a number of reasons, one of which being the coarse mesh used in the finite element analysis. It has been found that the friction is relatively insensitive to roughness, except at extremely low levels of roughness.

Dick and Cailletaud [19] have used finite elements to model a cylinder contacting a flat plate. Unlike the previously discussed references [14-18], this model is not of a single or multiple asperities, but rather a model of a macroscopic system. Displacement boundary conditions are used to put the cylinder, modeled in two dimensions, into contact with the plate. The plate, modeled in two dimensions as well, contains a surface layer with properties different than that of the plate substrate. Once contact has been developed the cylinder is locked and the plate is oscillated horizontally, with nodal forces in both normal and tangential directions being recorded. The ratio of the tangential to normal forces is then taken as the coefficient of friction. Different surface layers are analyzed using this technique to determine its effect on friction and are then compared to an analytical solution developed in the same source.

CHAPTER III

SURFACE PROFILOMETRY

Specimens

To facilitate the accurate modeling of the rail and slipper surfaces, samples of each were collected at Holloman Air Force Base and delivered to the University of Dayton. Table 1 shows a list of all the pieces received. While all the surfaces of the samples delivered to the University of Dayton were analyzed, not all were used in the finite element model. It was decided that due to a lack of available material data for certain pieces, as well as the extensive finite element analysis time spent on this project, only a single slipper-rail pair would be used. This pair consisted of the core from the Vascomax slipper (EDM Core) and the ¼" thick unused rail surface piece. These pieces can be seen in Figure 2. The EDM Core was used instead of the actual Vascomax slipper, because the physical dimensions of the slipper made it extremely difficult to place properly in the profiler. Also, the slipper was previously used during testing at HHSTT, while the EDM Core represented an unworn, or virgin, surface.

Part Description	Material	Used
Slipper	Vascomax	Yes
Core that was EDM'd out of Slipper	Vascomax	No
Slipper Insert	4130 Steel	Yes
Slipper Insert	4130 Steel	No
Rail Cross Section	1080 Steel	No
Rail Surface (1/4" thick)	1080 Steel	No

Table 1: Sample pieces received from Holloman AFB

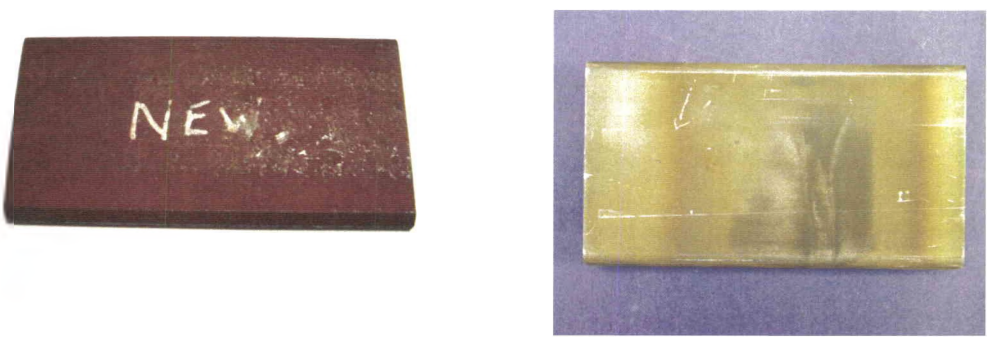

(a) (b)

Figure 2: (a) Unused rail section (b) EDM core

Profile Collection

In order to accurately describe the surfaces of the parts studied in this paper, the surface profiles of the pieces were measured. While multiple techniques are currently available to obtain surface profiles, two types of profilometers are prevalent: the stylus profiler and the optical profiler. The stylus profiler operates by physically dragging a stylus over the surface of a specimen, with the vertical deflection of the stylus recording the surface heights. Limitations exist with this method, as only two-

dimensional data can be obtained, and the radius of the stylus tip can limit its ability to detect very small scale roughness. More recently optical profilers, capable of three-dimensional analyses, have become available which record the way light is reflected off a surface in order to describe it, never physically touching the specimen.

For this study the Wyko NT8000 Optical Profiler (Figure 3) was used to obtain all the surface profiles. While the profiler is capable of sub-micron lateral resolution [20], such refinement of the surface was deemed unnecessary due to the practical modeling limits of the finite element software. Therefore a balance was needed between resolution and data size. It was determined that a combination of objective and field of view lenses which produced a 3.8 micron lateral resolution was sufficient to capture all the major features of the surfaces while allowing a maximum sample length. A finer description of the surface would shorten the total length of the profile, thereby lessening the number of major features included in the surface. Figure 4 shows the difference between the 3.8 micron resolution used and an approximately 1 micron resolution. All the key features are well defined in both while the finer resolution increased the number of data points by roughly a factor of four in each direction.

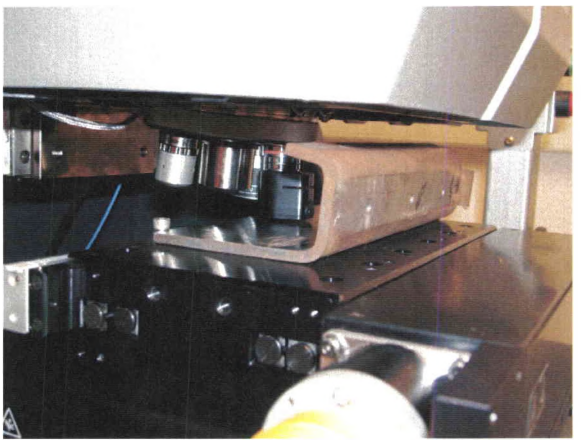

Figure 3: Wyko NT8000 Optical Profiler

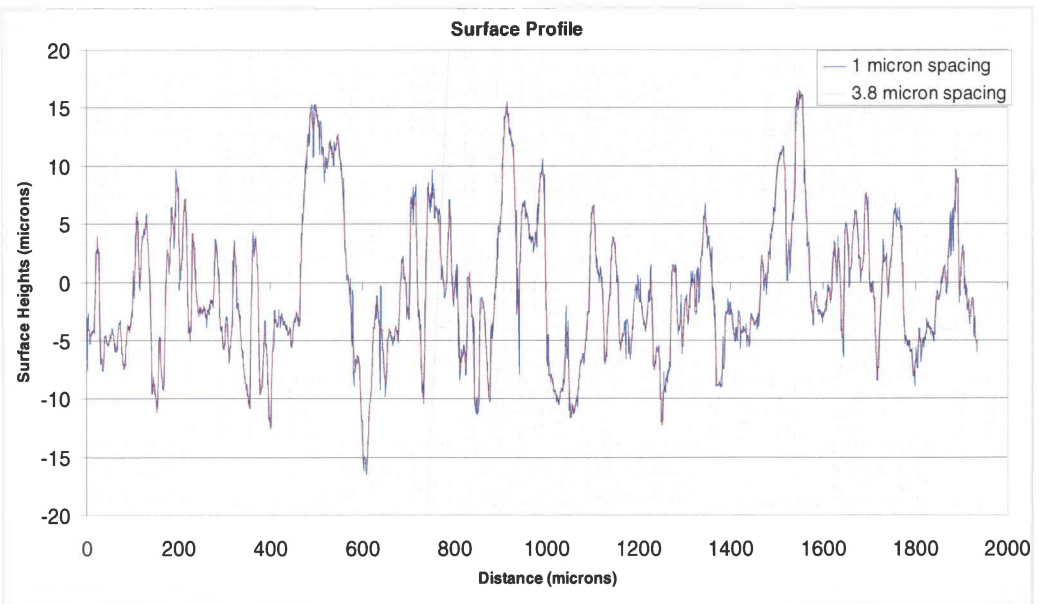

Figure 4: Surface profile at 1 and 3.8 μm lateral resolution

The Wyko NT8000 only has the capability to survey a maximum area of 8.45 mm x 8.45 mm in a single analysis [20]. Due to the parts' sizes, it was determined

that this would not be sufficient to effectively describe the surface. Instead, multiple profiles were taken from each part in different areas. The profiles of the EDM Core used 3 mm x 3 mm sampling areas, and those of the rail were 2.5 mm x 2 mm. Doing this provided a good account of the nature of the total surface of the part and decreased the chance that a localized feature would skew the overall profile description. The process of taking the profiles at different locations was automated with set distances between each measurement. Figure 5 shows the spacing of the measurements on the EDM Core and rail pieces. The Wyko NT8000 also utilized a built-in auto leveling routine which eliminated any tilt from the profiles, creating a horizontal mean line for each surface.

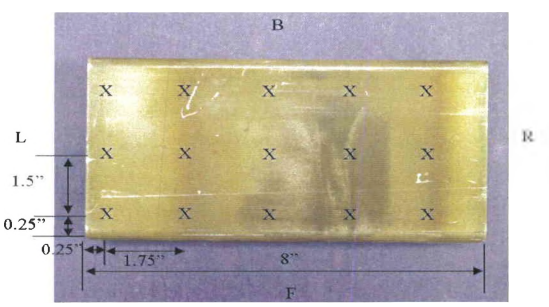

(a)

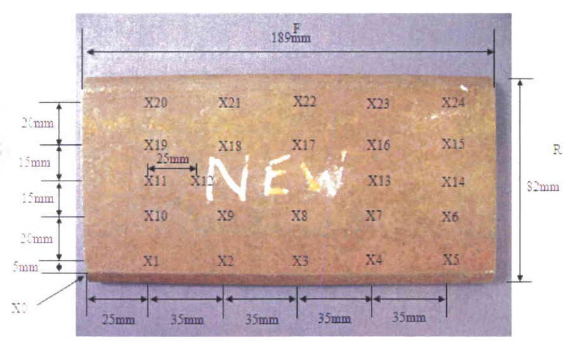

(b)

Figure 5: Sampling locations on: (a) EDM Core (b) Rail section

Profile Characteristics

In order to describe surface profiles, industry standards have been set which use numerical analysis to characterize their roughness. A large number of these standard parameters exist; however, some of the simpler and more widely used three-dimensional parameters are defined in Eqs. 1-5, where S_a is the average roughness, S_q is the root mean squared roughness, S_t is peak range, S_{sk} is the profile skewness, and S_{ku} is the profile kurtosis. For this study these will be the parameters used when describing the roughness of each surface.

$$S_a = \frac{1}{MN}\sum_{i=1}^{M}\sum_{j=1}^{N}\left|Z_{ij} - \bar{Z}\right| \tag{1}$$

$$S_q = \sqrt{\frac{1}{MN}\sum_{i=1}^{M}\sum_{j=1}^{N}\left(Z_{ij} - \bar{Z}\right)^2} \tag{2}$$

$$S_t = S_p + S_v \tag{3}$$

$$S_{sk} = \frac{1}{MNS_q^3}\sum_{i=1}^{M}\sum_{j=1}^{N}(Z_{ij} - \bar{Z})^3 \tag{4}$$

$$S_{ku} = \frac{1}{MNS_q^4}\sum_{i=1}^{M}\sum_{j=1}^{N}(Z_{ij} - \bar{Z})^4 \tag{5}$$

Once the surface profiles were taken from each of the rail and slipper pieces, their parameters were calculated individually for each scan section. This was done using the commercially available software *ImageJ*, along with a plug-in *Open OPD*, created by Nilesh Powar of University of Dayton Research Institute. The plug-in is able to read and analyze three dimensional profile data produced by the Wyko

NT8000. The parameter averages were then calculated to determine overall parameters for the pieces.

For comparative purposes Figure 6 shows typical R_a parameter values for engineered parts. The R_a parameter is the two-dimensional equivalent of S_a. As can be seen, the EDM Center piece used in this study, with an average S_a value of 5.79 μm, falls on the rougher end of the range for most EDM parts. The rail piece studied shows a rougher overall surface with an average S_a value of 10.02 μm.

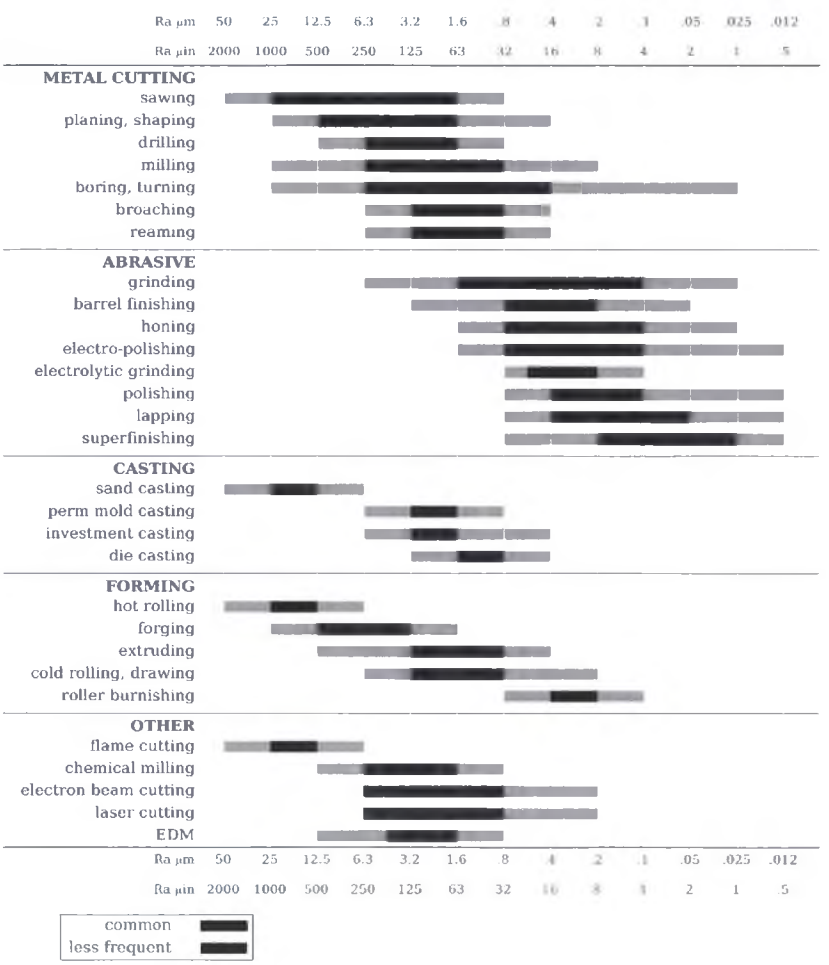

Figure 6: Typical R_a roughness parameters for engineered parts

Transforming 3-D Profiles to 2-D Profiles

While statistical data is helpful in characterizing the surfaces of the parts, ultimately two-dimensional profiles must be obtained for use in the finite element analysis. The process started by opening an individual surface profile from the piece being analyzed in *ImageJ*. A sample of the plot can be seen in Figure 7(a) with the x and y axes corresponding to the longitudinal and transverse axes on the part, and the shading of the plot representing the z axis, or height. Figure 7(b) shows an actual three-dimensional plot from the same data.

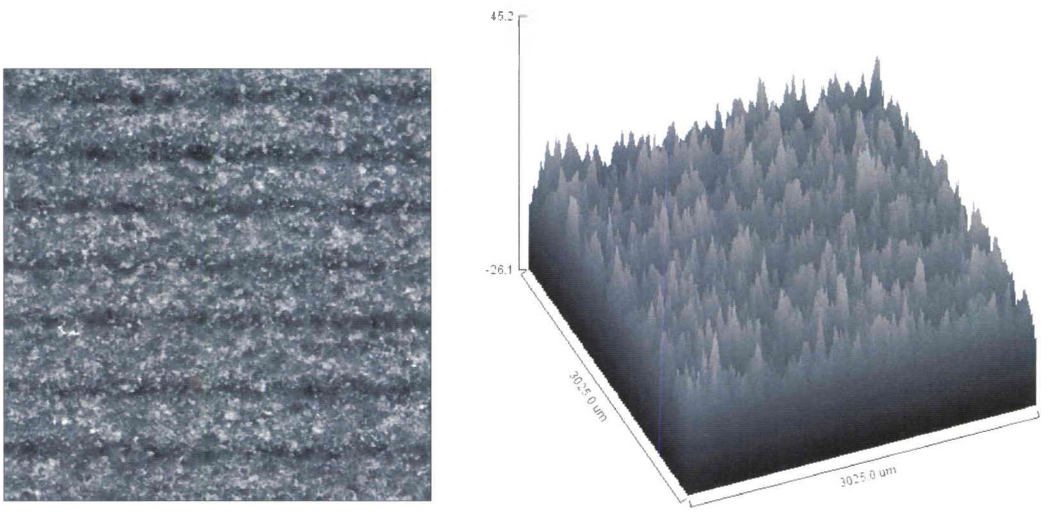

(a) (b)

Figure 7: *ImageJ* surface plots in: (a) two dimensions (b) three dimensions

In order to isolate the profile in the longitudinal direction a straight line was made through the plot with a constant y coordinate. The x and z coordinates were

then recorded to give a two-dimensional output for the surface. The statistical parameters of the two-dimensional profiles obtained were compared to the overall three-dimensional values calculated for the entire part to ensure agreement between them. Four profiles from each piece were used to create four unique pairs of EDM Core and rail models.

Profile Filtering

One major aspect of this study was to establish a relationship between surface roughness resolution and its effect on frictional sliding. In order to accomplish this, a low-pass spatial filter was used to progressively smooth out each of the two dimensional profiles. Effects from this smoothing could then be determined through the finite element analysis. The filtering program employed a Fast Fourier Transform routine to break down the surface profiles into a series of spatial frequencies and then allowed for the removal of any desired frequency, called the cut-off frequency (Ω_c), and all higher frequencies. With the progressive lowering of the cut-off frequency, the profiles became smoother.

Each cutoff frequency used in the filtering program is directly related to a spatial wavelength. Eq. 6 shows the relationship between the cutoff frequencies and their corresponding spatial wavelengths (λ_c). These wavelengths indicate the shortest half sine wave retained in the filtering process. Table 2 shows the cutoff frequencies used and the corresponding smallest wavelength subsequently retained.

$$\Omega_c = 1/\lambda_c \tag{6}$$

	Filter 1	Filter 2	Filter 3	Filter 4	Filter 5
Ω_c (Hz)	0.02	0.01	0.005	0.0025	0.001667
λ_c (μm)	50	100	200	400	600

Table 2: Cutoff frequencies used for filtering profiles

To assess the effect of varying model resolution on the finite element predictions, both slipper and rail surfaces were filtered at the same cutoff frequency simultaneously. Once filtered, these new surfaces were combined to form new models and entered into the finite element software in a similar fashion as the original surfaces.

CHAPTER IV

FINITE ELEMENT ANALYSIS

Analysis Type

The current study utilizes two-dimensional plane-strain models to simulate the rough surfaces of the rail and slipper. While ABAQUS is capable of three-dimensional analysis, using plane-strain assumptions to simulate the third dimension significantly reduces the number of elements needed to model the surfaces. The finite element software ABAQUS Explicit [21] has been used to run dynamic analyses of the slipper rail interaction.

Geometry

The finite element pre-processor software ABAQUS CAE is used to model the EDM Core (representing the slipper) and rail pieces. The two-dimensional surfaces profile data is imported into ABAQUS CAE as a series of line segments. Collectively the line segments form the horizontal contacting surface measuring approximately 2 mm (or .078 in) in length. Each piece is given a vertical depth of .1 in to form a two-dimensional rectangular piece, with one rough edge. The large depth compared to surface asperity size allows the interactions at the rough surface to be isolated from the effects of applying boundary conditions at the opposite surface.

Each model consists of one slipper part and one rail part. However, the rail part is copied and merged with itself multiple times to create a longer repeating rail surface. The complete setup of the slipper/rail model can be seen in Figure 8.

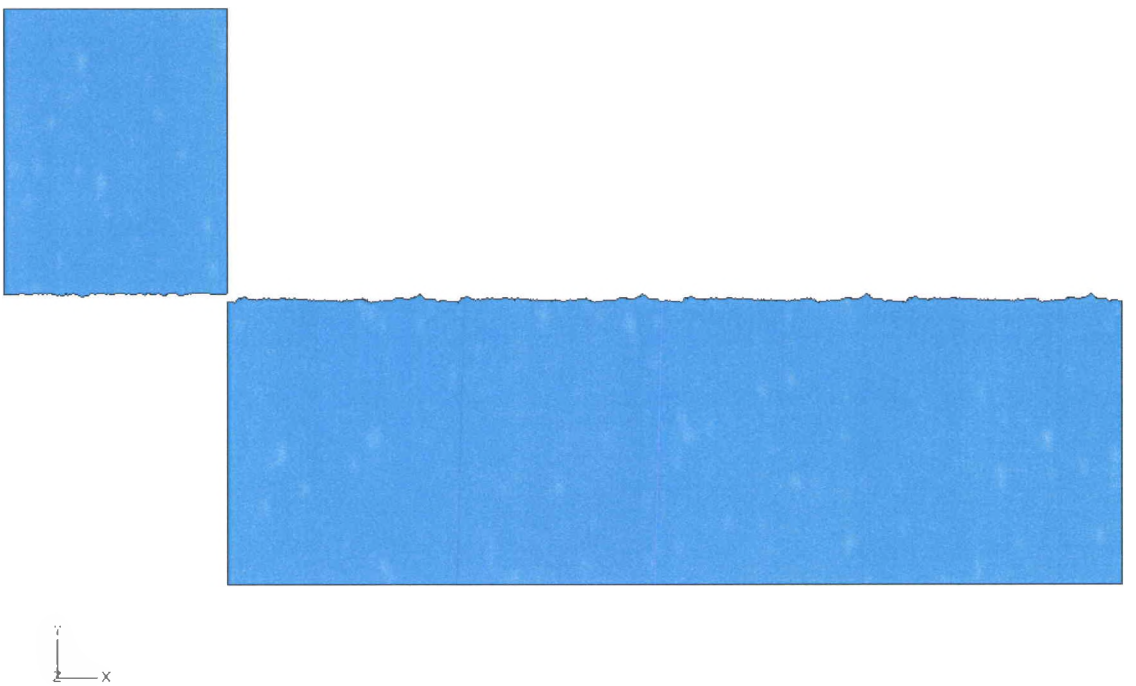

Figure 8: ABAQUS slipper/rail model layout

Material Properties

Both slipper and rail pieces in this study are steel, with the slipper being made from Vascomax 300 steel and the rail being composed of 1080 steel. Each is modeled as isotropic elastic-plastic in ABAQUS. The elastic properties, determined in [22], of both materials can be seen in Table 3. Plasticity data, also provided in [22], is defined in the form of the Johnson-Cook model. This is a widely used

constitutive model in high energy dynamic analysis, and can be seen in Eq. 7. The model calculates flow stress (σ) in terms of strain (ε), but also takes into account variables such as strain rate ($\dot{\varepsilon}^*$) and temperature variation (T^*), although the temperature variable was ignored for this study. Constants for the Johnson-Cook equation can be seen in Table 4 for both Vascomax 300 and 1080 steel.

Material	E (Msi)	v
Vascomax 300	26.2	0.27
1080 Steel	29.4	0.27

Table 3: Elastic properties

$$\sigma = \left(A + B\varepsilon^{n}\right)\left(1 + C \ln \dot{\varepsilon}^{*}\right)\left(1 - T^{*m}\right) \tag{7}$$

Coefficients	Vascomax 300	1080 Steel
A (Gpa)	2.1	0.7
B (Gpa)	.124	3.6
C	0.03	0.17
m	0.8	0.25
n	0.3737	0.6

Table 4: Johnson-Cook coefficients

Once the Johnson-Cook coefficients for the different materials are applied to the model, a series of Stress-Strain curves are developed for varying strain rates and entered into ABAQUS as isotropic hardening data.

While compiling the stress-strain data for 1080 steel, it was discovered that the strain hardening generated by the model was excessively high, so much so that the validity of the material model became questionable. Mises stresses on the order of 600 - 800 ksi were being experienced in preliminary simulations, while the static yield stress was only approximately 100 ksi. Therefore, to remedy the unrealistic hardening, the 1080 steel material model is set to elastic-perfectly plastic, with a yield stress of 101.525 ksi.

During frictional sliding, it is accepted that some material on the surfaces will fail and create debris particles. While ABAQUS has tools capable of simulating this event, no failure criteria are used. This is due to lack of an accurate failure model for either material, along with the major complications failure modeling creates with contact formulations within ABAQUS.

Contact Interaction

An important part of this study is the contact interaction between the slipper and rail surfaces. By default surfaces in ABAQUS do not interact with each other, but rather a contact formulation must be specified. For this situation ABAQUS Explicit offers two distinct contact formulations: general contact and contact pair. The contact pair algorithm is used in this study, since general contact, while more robust, is not available for two-dimensional analysis. It is important to note that element based contact is used, not node based.

Both slipper and rail surfaces are modeled using deformable continuum elements, which allow the use of a balanced master-slave kinematic contact algorithm

within the contact pair formulation. This algorithm is the most conservative and therefore accurate of the options available in ABAQUS for this study. While requiring slightly more computational time, the need for accuracy dictated this approach.

When using any interaction available in ABAQUS, interaction properties must be applied as well. For the contact interaction a normal and tangential property must be assigned. In this study the default "hard" contact relationship is utilized in the normal direction. The pressure-overclosure relationship is again the most conservative option available, minimizing the penetration between surfaces. The tangential contact property required in ABAQUS is the frictional property. Such a property facilitates how the shear components operate between the contacting surfaces. The basic Coulomb friction interaction available in ABAQUS is used, with the coefficient of friction being one of the variables studied.

Element Type

Elements in this study consisted of a combination of 3-node and 4-node reduced integration plain strain continuum elements. These are two-dimensional elements which in ABAQUS are referred to as CPE3R and CPE4R [21]. Continuum elements are the general purpose, standard volume elements offered in ABAQUS. The reduced integration prefix indicates the number of integration points used. Figure 9 shows these elements.

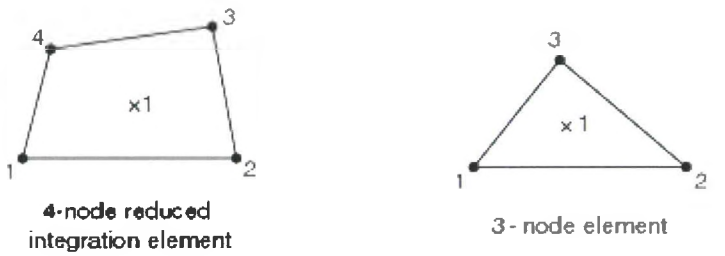

Figure 9: 4-node and 3-node reduced integration elements

The reduced integration elements are used for the analysis because the contact pair formulation in ABAQUS Explicit requires it. They are commonly referred to as constant strain elements, as gradients are unable to be captured. Although computational time is lessened by using these elements, proper meshing in high strain gradient regions is crucial. Throughout all of the parts the majority of the elements are 4-node quadrilaterals, with typically around 3.5 percent being triangles. The triangular elements are included only to help the meshing algorithm since the non-uniform geometry of the rough contacting surfaces make it difficult to exclusively use the quadrilaterals.

Meshing Technique

As stated, proper meshing is required in high stress/strain gradient areas. In order to do this, each part is partitioned into sections. Different mesh seedings are established at these partitions in order to create a variable mesh density throughout the part, with the highest mesh density occurring at the contacting surfaces of the parts. This technique is the only way to retain a dense mesh at the surfaces while

keeping the total number of elements to a minimum. Figure 10 shows the mesh of one of the unfiltered slipper parts. The rail parts are meshed with the same density variation as the slipper, with an approximate mesh spacing of 2 μm at the surface.

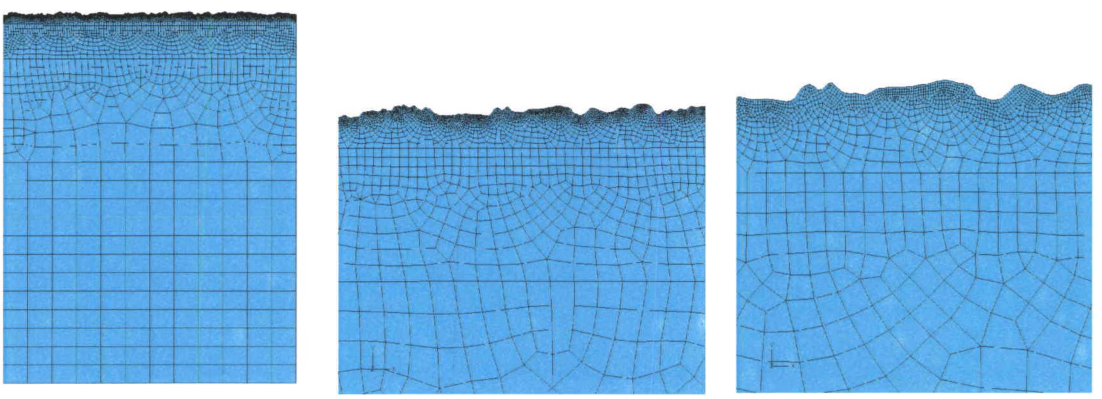

Figure 10: Meshing on slipper part at varying magnifications

Special Purpose Analysis Techniques

The analysis in this study requires some special techniques in order to be completed. One of the major techniques utilized is mass scaling. Mass scaling is typically used in ABAQUS Explicit for either quasi-static analysis or dynamic analysis where inertial effects aren't important. In general, mass scaling increases the density of certain elements in order to increase their stable time increment, which, in turn reduces analysis run time as fewer increments are needed.

To determine the stable time increment, the wave speed of the element is first approximated as in Eq. 8, where E is the elastic modulus and ρ is the density. This is then used in conjunction with the element's shortest physical dimension (L_{min}) to determine the element's stable time increment (Δt) in Eq. 9.

$$c_d \approx \sqrt{E/\rho} \tag{8}$$

$$\Delta t \approx \frac{L_{min}}{c_d} \tag{9}$$

The need for a dense mesh at the surfaces of the parts requires some elements to be incredibly small. This in turn makes Δt so small that the computation time needed to run an analysis becomes unrealistically long. By artificially increasing ρ via mass scaling, the increment size becomes large enough for the analysis to be run. It is determined that the mass scaling definitions be set to update throughout the analysis to compensate for the high deformations that occur, which would also bring Δt down to unmanageable levels.

A sample test was run to find where to set Δt without it having adverse affects on the force results. Figure 11 shows the vertical reaction force data of a sample analysis where the slipper part was slowly "pressed" against the rail part at differing Δt's. From this it is determined to set $\Delta t = 10^{-6}$ seconds. This reduces Δt four orders of magnitude from the original 10^{-10} seconds required in some models.

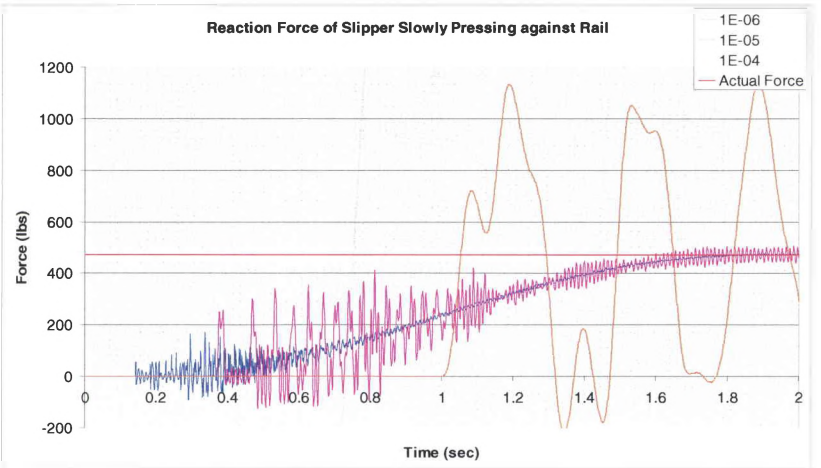

Figure 11: Vertical reaction force of a sample analysis at varying Δt's

Model Setup

Reference points are used in the ABAQUS model to facilitate accurate boundary condition application and data retrieval. These reference points do not represent any part of the solid geometry and therefore have no physical properties. Both slipper and rail parts are assigned a reference point which is tied to portions of their geometry using the linear constraint equations available in ABAQUS. This constraint can be seen in Eq. 10, where u_i^P is the nodal variable (displacement in this case) at node P, i is the degree of freedom, and A is a general coefficient. Setting A_1 and A_2 equal to 1 and -1 respectively tie the displacements of the selected nodes of the part to the reference point. Both horizontal (u_x) and vertical (u_y) translational degrees of freedom are constrained in this way. The geometry which is selected for each piece can be seen in Figure 12.

$$A_1 u_i^P + A_2 u_j^Q = 0 \qquad \textbf{(10)}$$

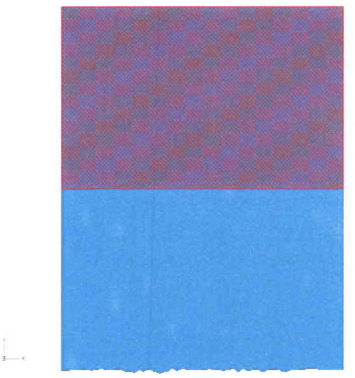

(a)

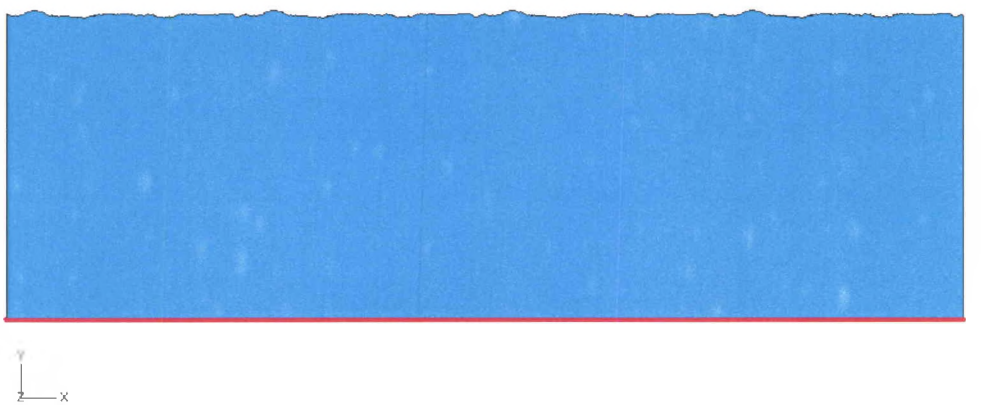

(b)

Figure 12: Selected geometry tied to reference points on (a) slipper (b) rail

With the selected nodes and reference points coupled together, boundary conditions are applied directly to the reference point. The rail's reference point is assigned a 'fixed' or zero displacement/rotation BC in all directions, which ensures the rail remains stationary throughout the simulation. The slipper reference point is assigned a zero displacement BC in the vertical direction to keep a constant

separation between the rail and slipper. A zero rotation BC is applied as well to ensure the slipper stay completely horizontal during simulations. It is then applied a constant velocity BC in the horizontal direction to simulate the slipper sliding over the rail surface.

In order to determine the proper vertical deflection of the slipper relative to the rail, preliminary simulations are run in order to relate the separation of the surfaces to an overall mean pressure. These simulations consist of the slipper being slowly displaced downward onto the rail, with the vertical reaction force being recorded. Multiple simulations are run with the slipper piece being located at different spots on the rail each time to represent the different contact conditions between the surfaces. The average forces are taken for each model and provide a load-deflection curve which is used to determine precisely what separation to use when running the sliding simulations. Also, the separation could be changed for a given model to represent pressure variations. The load deflection curves can be seen in the *Results and Discussion* section, and an overview of the process to determine them can be seen in Figure 13.

During the sliding simulations reaction force data is taken from the rail reference point in order to record the normal and tangential forces experienced by the rail during the sliding simulation. This data will be analyzed to determine the frictional behavior occurring during the simulation. An overview of the sliding simulation procedure can be seen in Figures 14.

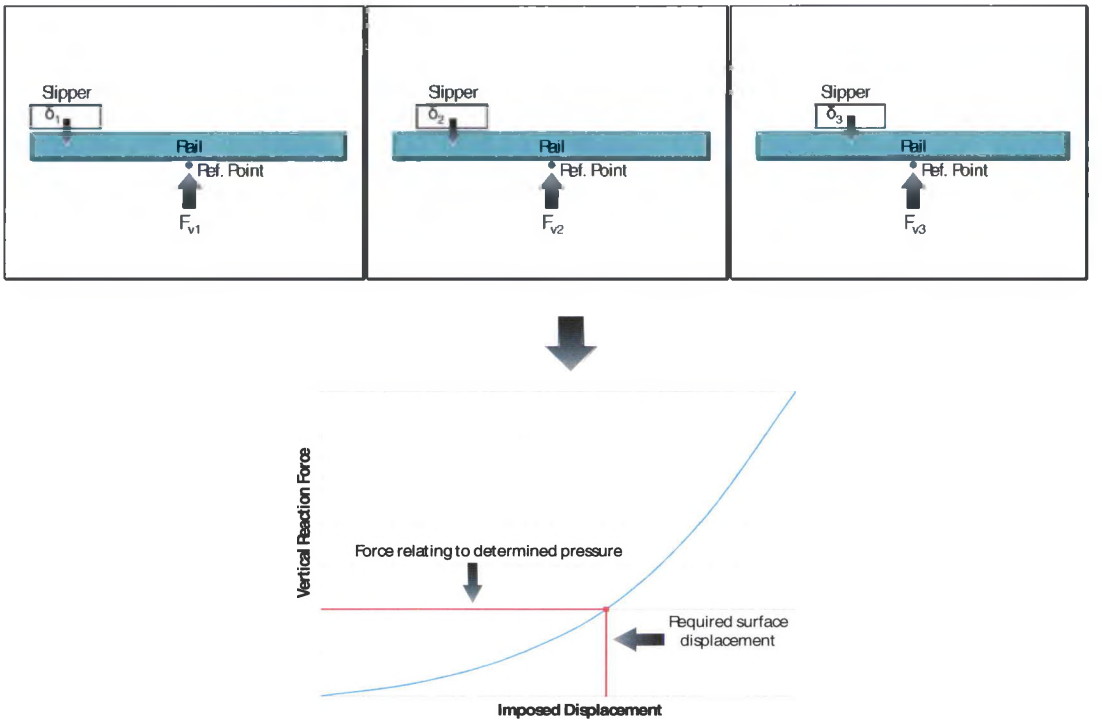

Figure 13: Preliminary simulation overview

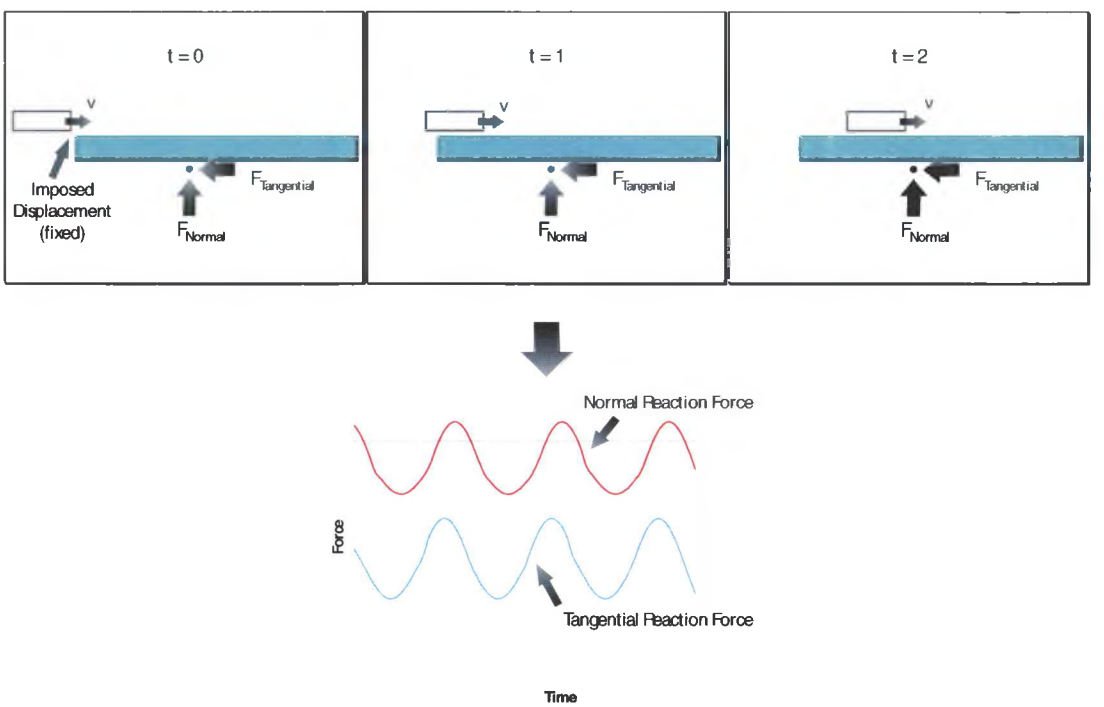

Figure 14: Sliding simulation overview

CHAPTER V

RESULTS AND DISCUSSION

Four profiles were taken from both the slipper and rail surfaces and imported into ABAQUS to represent the solid geometry of the parts which they were taken from. Each profile was randomly paired with one of the profiles from the opposite piece to create four individual models of the contacting surfaces. Each model was filtered multiple times using the low-pass filter described in the *Surface Profilometry* section with the effect on the friction coefficient being recorded for each individual model. Also, studies of the effects of internal model friction, velocity, and normal pressure were also conducted on a portion of the four total models.

Profile Filtering

The results from the filtering process can be seen in Figures 13-16. The slipper surfaces show a smaller range of heights but contain more total 'asperities' or local peaks. The rail surfaces on the other hand are generally characterized by only a few larger peaks. Overall, the filtering process impacted the profiles in two distinct ways. First, the peaks were lowered or flattened, and secondly, each peak's curvature was reduced with an increase in filter length. When looking at the profiles with more

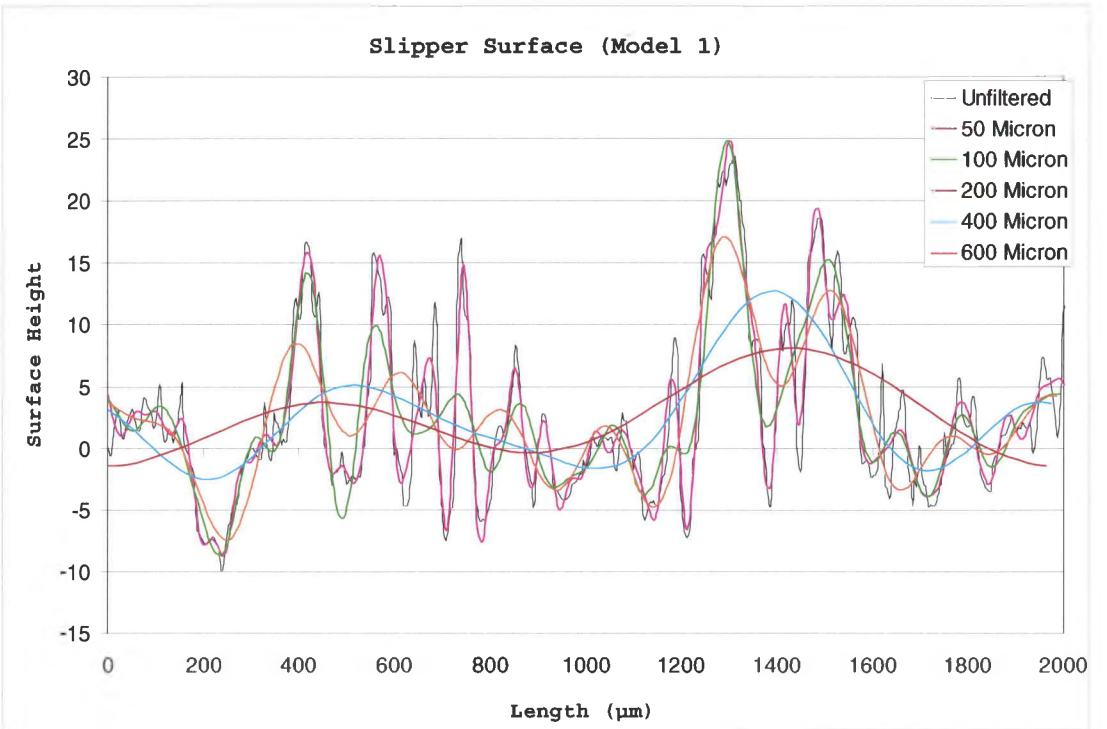

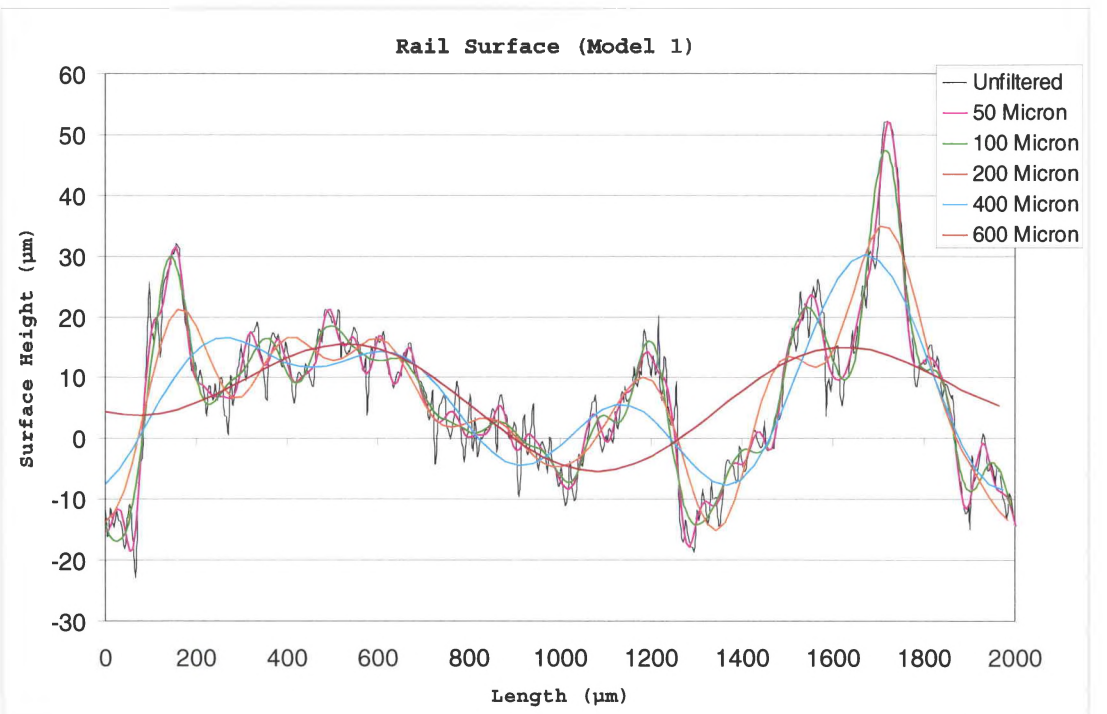

Figure 15: Model 1 surface profiles at varying filter levels

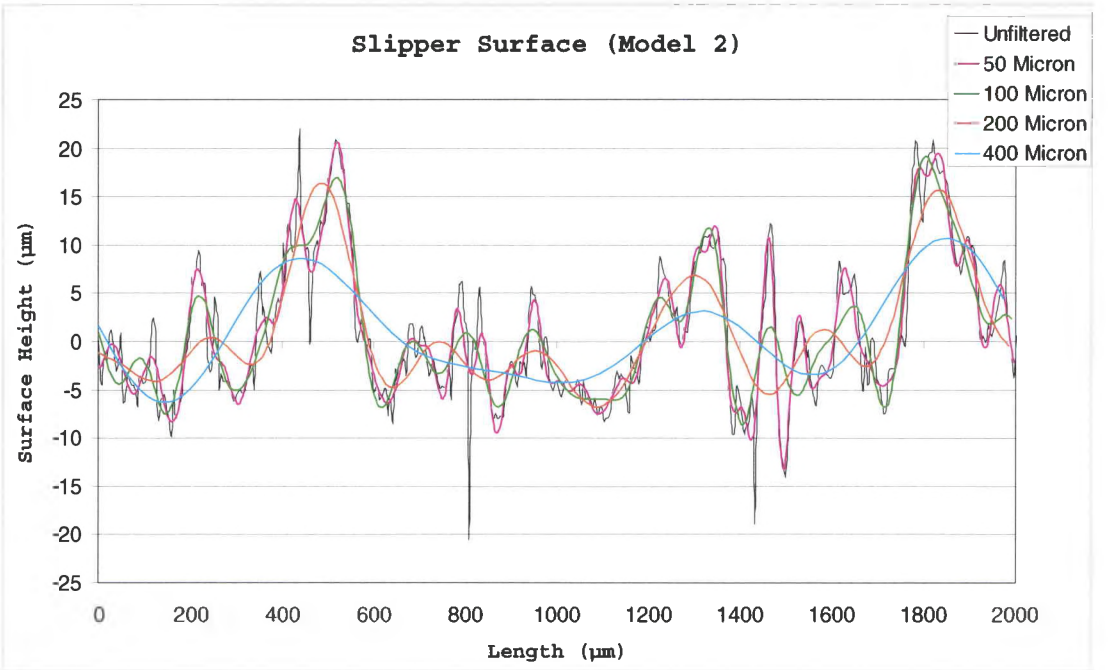

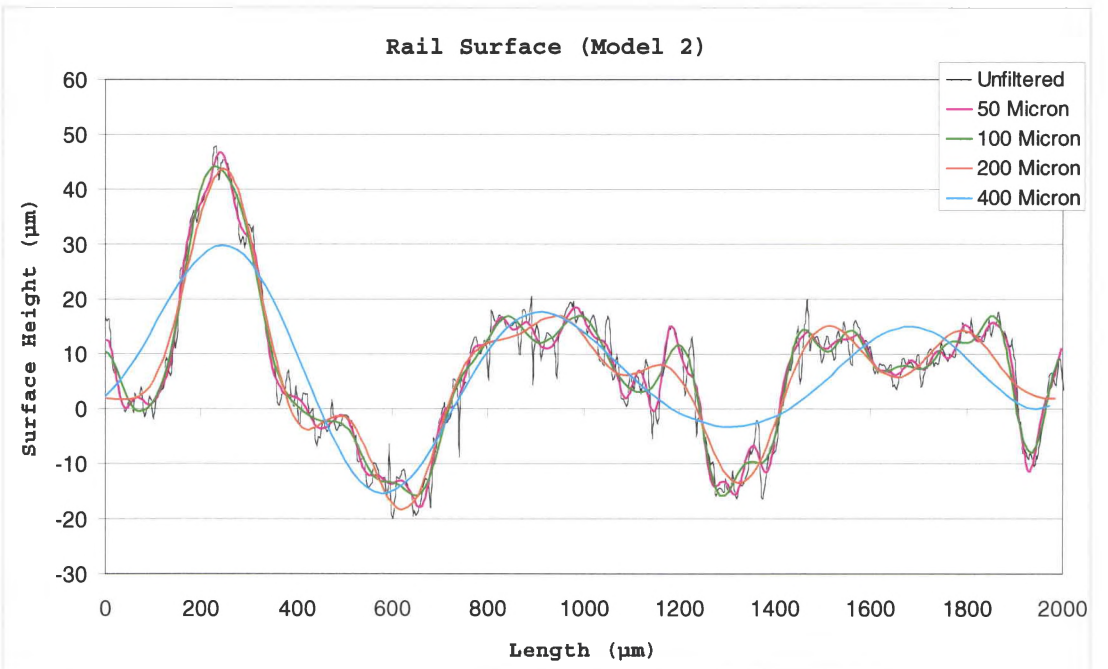

Figure 16: Model 2 surface profiles at varying filter levels

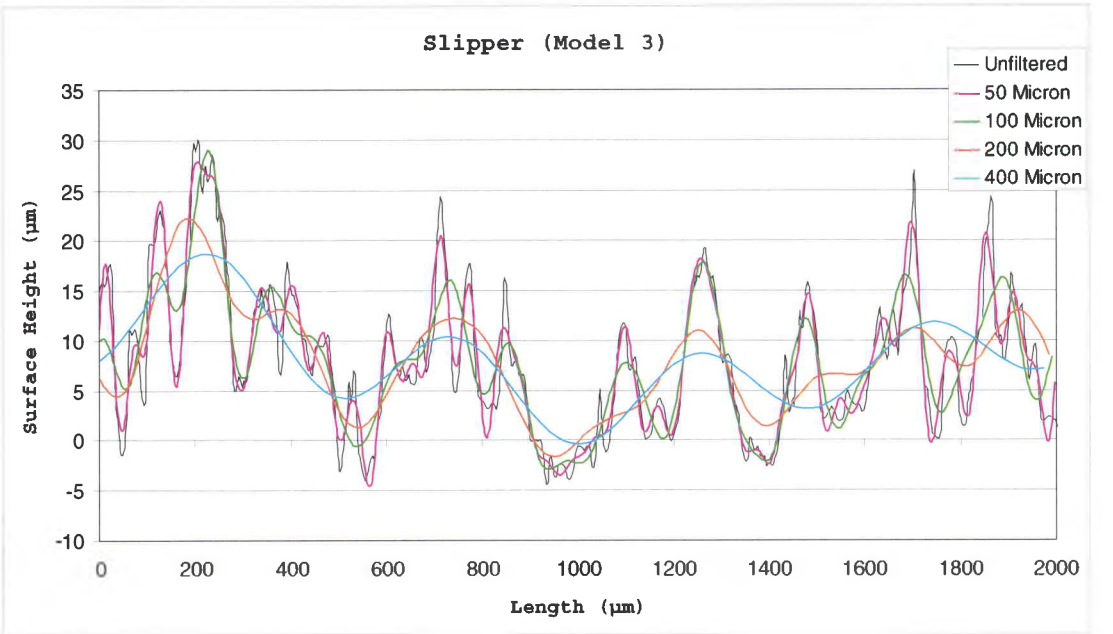

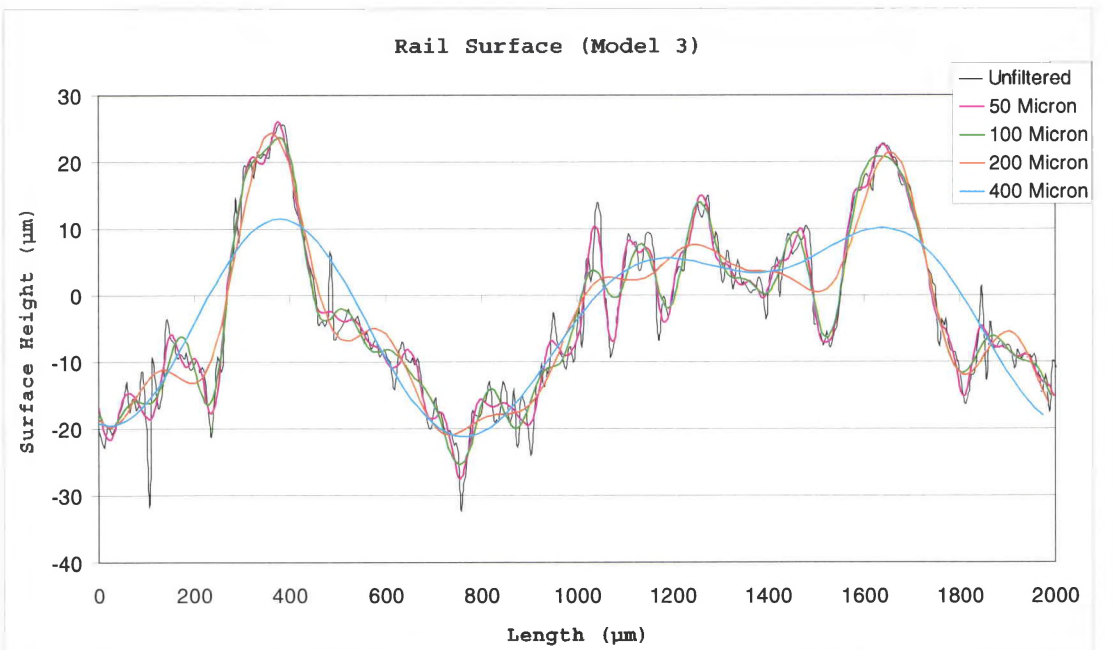

Figure 17: Model 3 surface profiles at varying filter levels

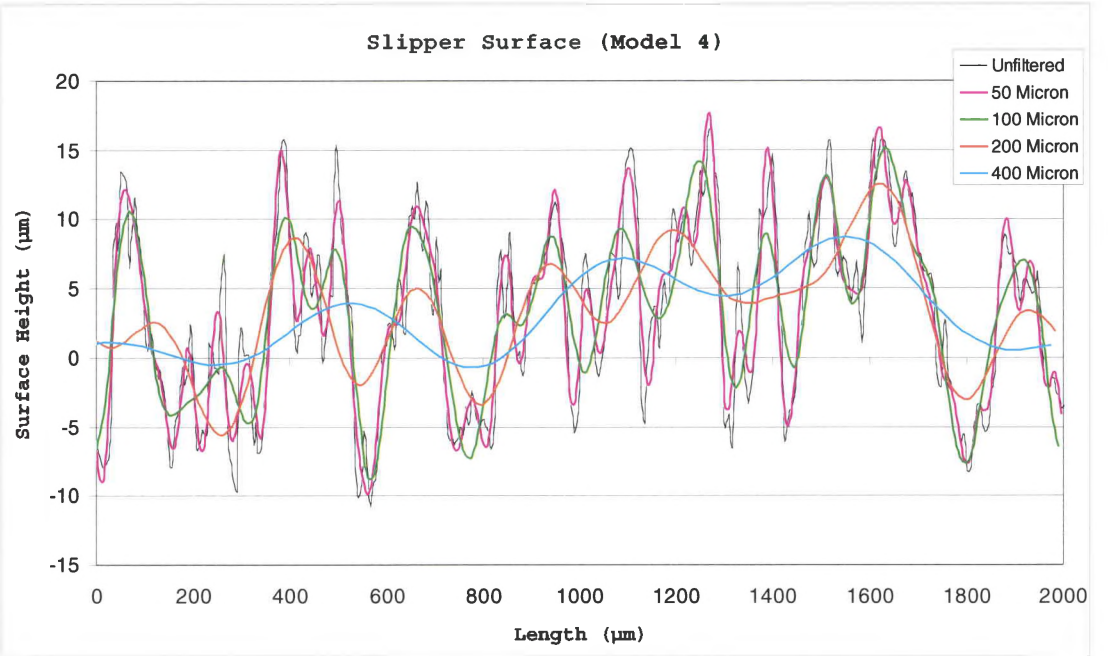

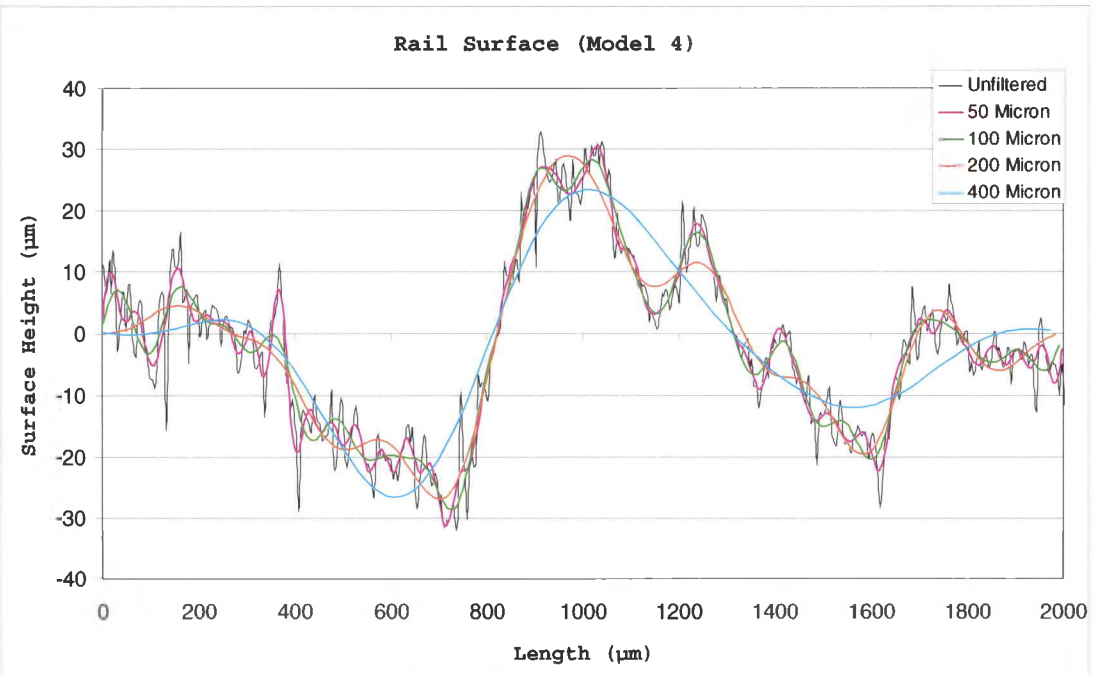

Figure 18: Model 4 surface profiles at varying filter levels

detail, however, it can be seen that the filtering process affected the profiles differently based on each profile's specific geometry. For example, model 1's rail surface retained its major features only through the 100 micron filter, where in models 2 and 3, the rail's dominant features are still apparent up until the 400 micron filter.

Again looking at the profiles in a broad scope, it can be seen that due to the frequency of local asperities, the slipper surface is altered more from the filtering than the rail surfaces. While the curvature of the large asperities on the rail surfaces is lessened, a real decrease in major asperity height is not experienced until a larger filter is used. Alternately, in the slipper surfaces, a decrease in asperity height is experienced sometimes with even the 50 micron filter, but typically no later than the 100 micron filter.

Mean Pressure Determination

The pressure displacement curves used to set up each model's sliding simulation can be seen in Figures 17 & 18. These represent the relationship between physical separation of the surfaces and the overall vertical load and therefore mean normal pressure applied. In each of the models the overall trend was for the curve to become steeper as a larger filter (creating a flatter surface) was used. Some variations were experienced in this overall trend. Model 1 showed relatively little difference between the unfiltered and 50 μm model with the 100 μm model acting contrary to the overall trend of becoming steeper with larger filters. Model 2 exhibited grouping for unfiltered and 50 μm models as well as the 100 and 200 μm models. Models 1

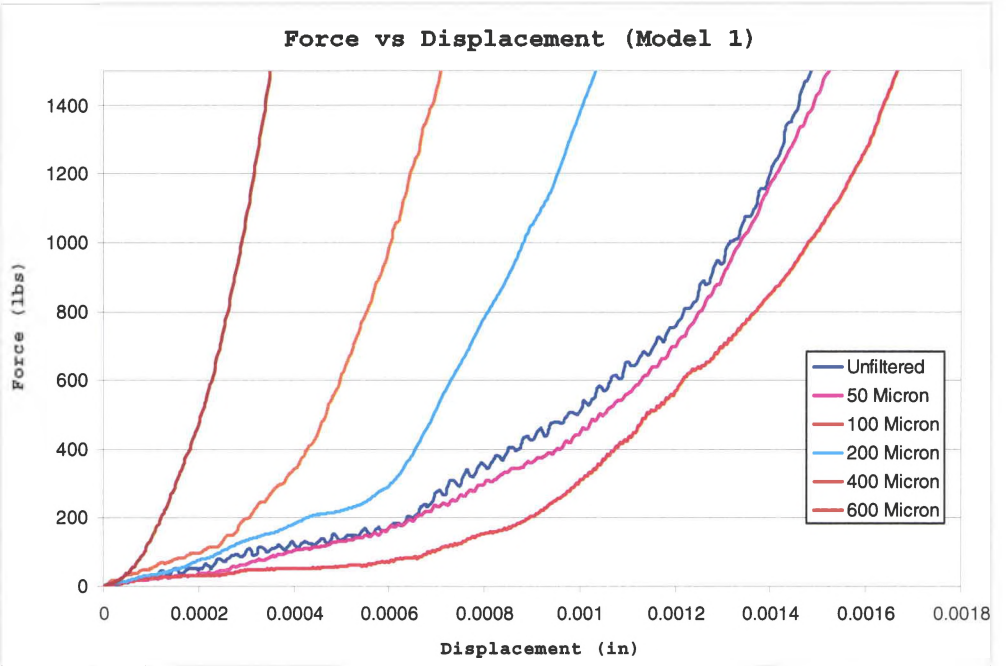

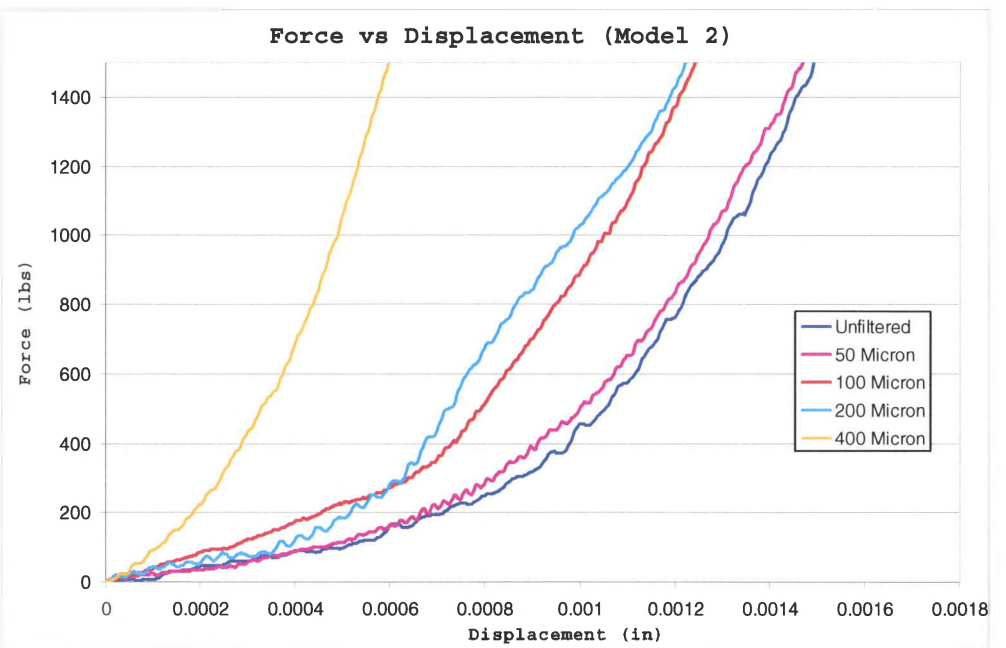

Figure 19: Vertical force-deflection curve for models 1 and 2

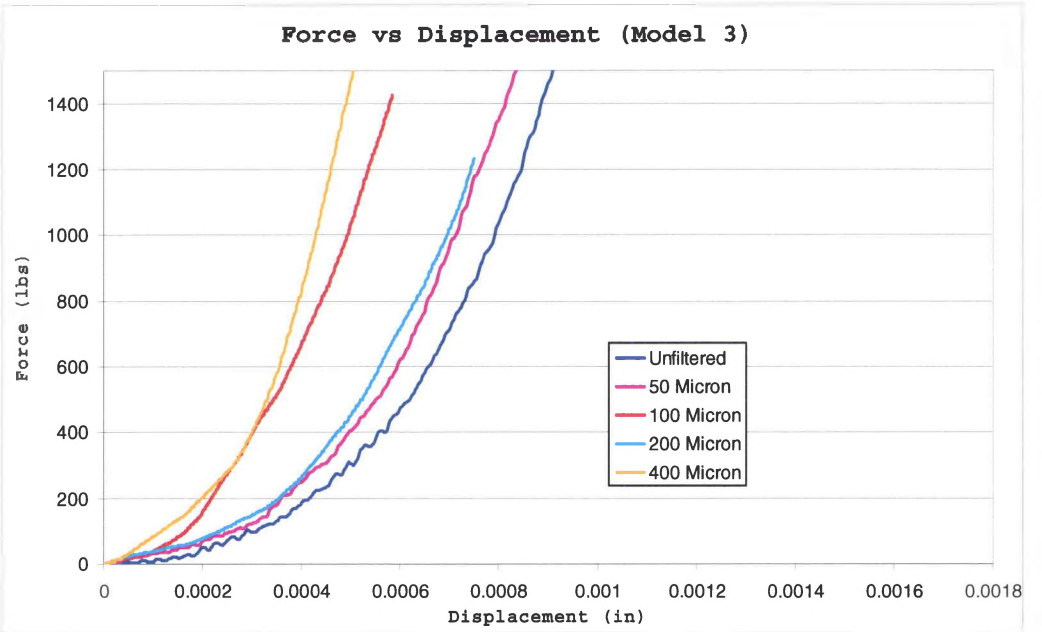

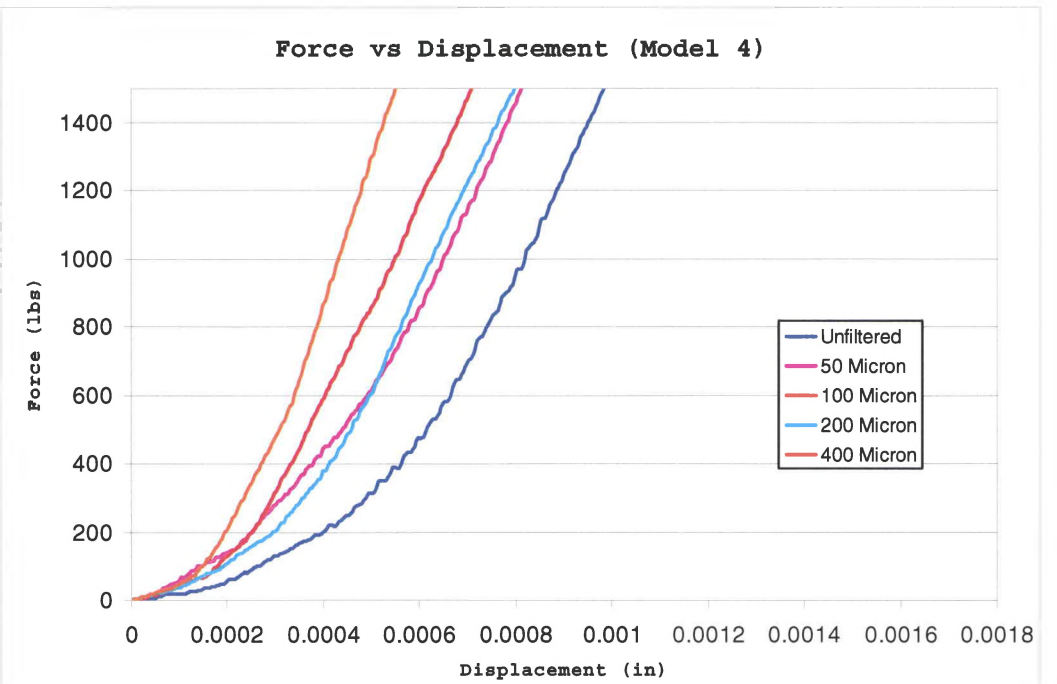

Figure 20: Vertical force-deflection curve for models 3 and 4

and 2 also exhibited a smaller force per displacement compared to models 3 and 4, with a larger separation between the different filtering levels as well. Another trend of the curves is for them to start out non-linear and continue to become somewhat more linear as the displacement increases. This was due to an increasing number of asperities coming into contact in the initial stages of the contact. Once enough contact areas were formed the curves moved to a more linear form, representing the crushing of these major asperities.

Force Results & Model Deformation

In order to derive a "measured" coefficient of friction from the sliding simulations in Abaqus, a time average of the force resultants were taken from the reference point tied to the rail. Both normal and tangential force data were taken, with the frictional coefficient being considered the tangential force divided by the normal force. Figures 19-22 show the results for the simulations for model 1 at the varying levels of filtering. The tangential force is negative on the graph while the normal force is positive. This was simply a product of the model geometry along with the default coordinate directions Abaqus uses. It can be seen that true contact is not experienced throughout the entire simulation, represented by the zero (or average zero) force portions of the graphs. Only when the larger asperities came into contact, represented by the peaks, did the surfaces actually touch one another. Since the 2 mm long rail surface was repeated multiple times to create the longer total rail surface, a high degree of repetitiveness can be seen in each of the graphs as expected. The scatter of the data

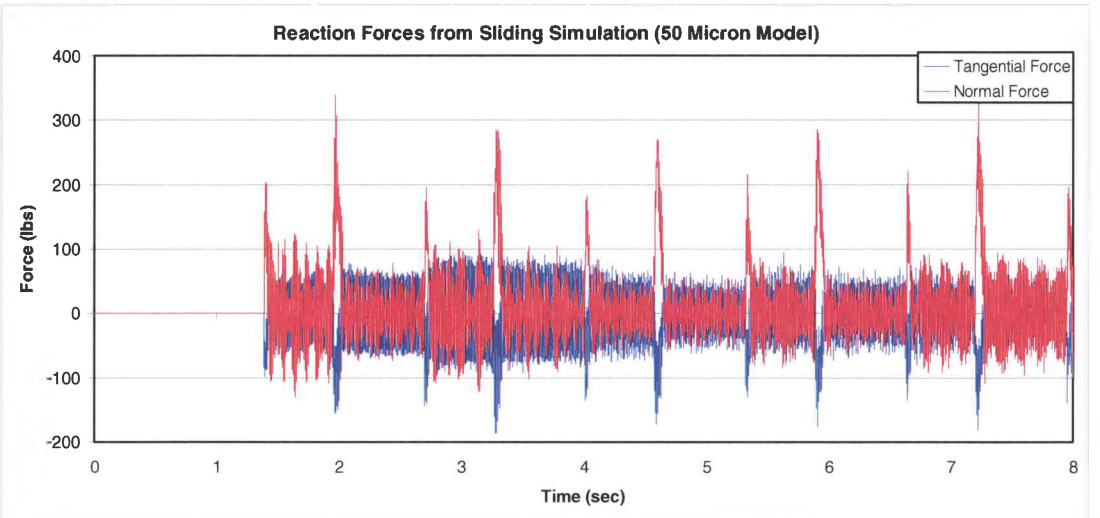

Figure 21: Force resultant from model 1 (50 μm) sliding simulation

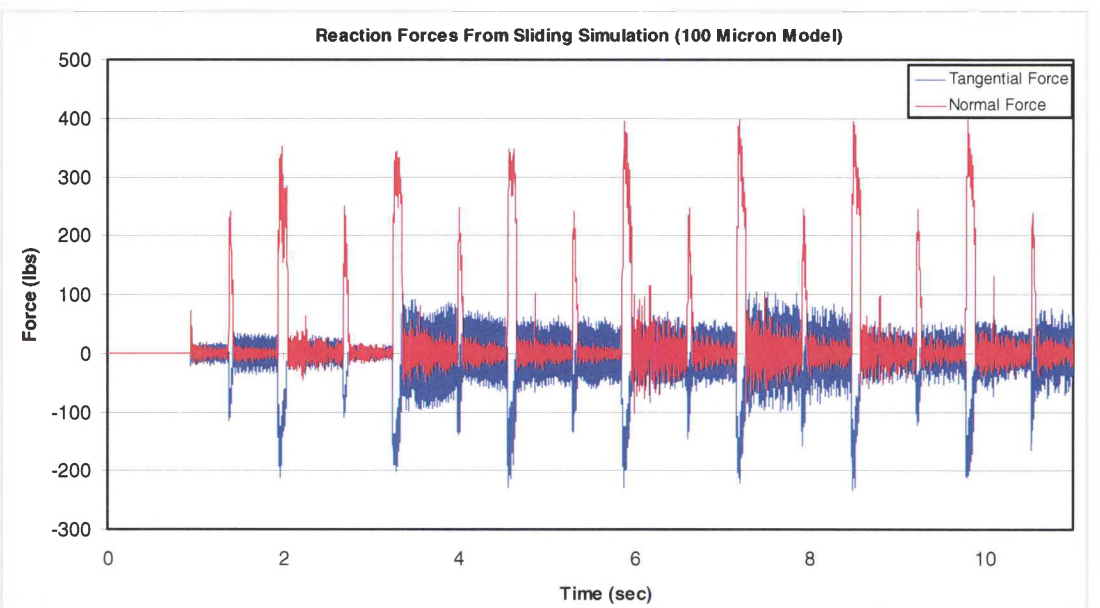

Figure 22: Force resultant from model 1 (100 μm) sliding simulation

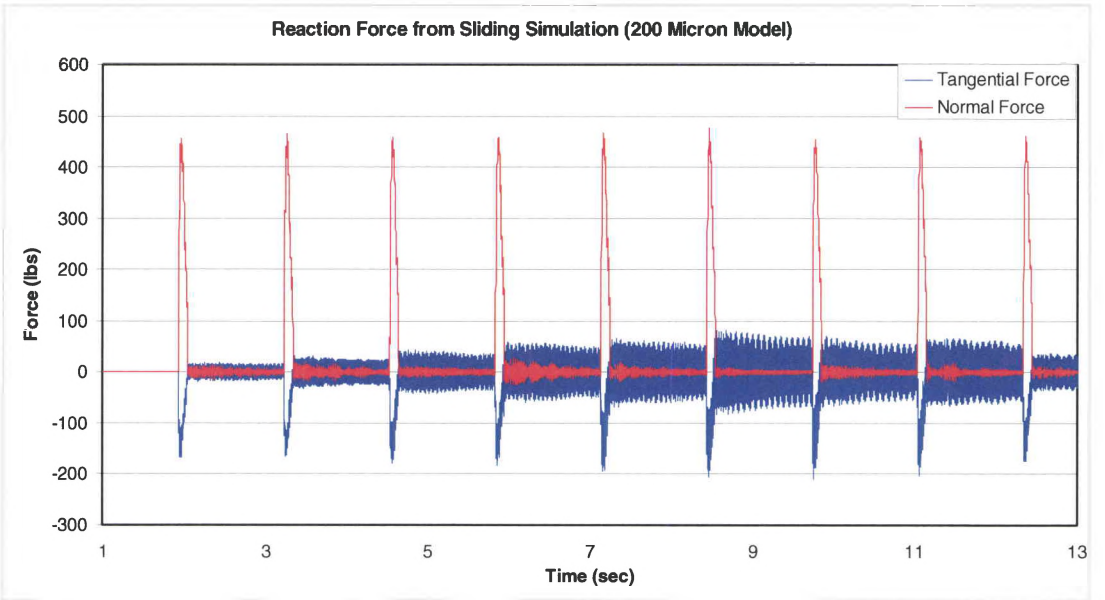

Figure 23: Force resultant from model 1 (200 μm) sliding simulation

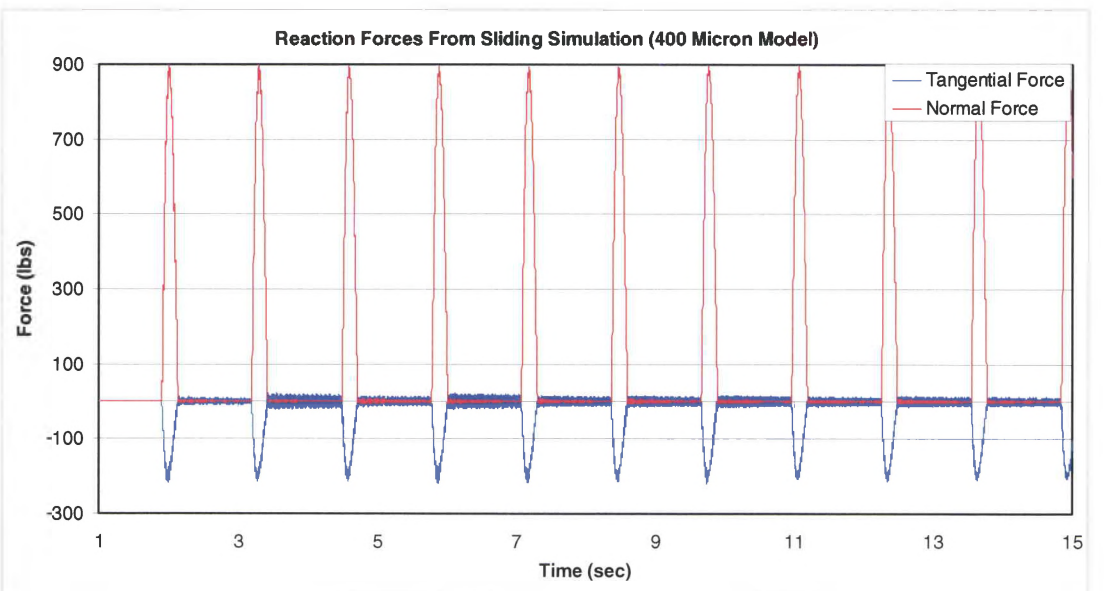

Figure 24: Force resultant from model 1 (400 μm) sliding simulation

seen in each graph is due to the fact that a dynamic solution was used, which inherently produces some scatter. Since the averages of the forces were recorded, the scatter did not prove detrimental to the analysis. The finer models, the 50 μm and 100 μm models in this case, display more peaks in their force graphs which is indicative of the fact that more of the surface geometry is present and coming into contact. The force graphs of the smoother models contain fewer peaks, albeit larger ones. This is due to the asperities contacting each other being more massive, yet much less frequent.

As the filters became larger, the type of deformation changed from highly plastic to mostly elastic. Figures 23-25 shows the equivalent plastic strain for the same pair of the contacting asperities from Model 2 filtered at 50 μm, 100 μm, and 400 μm respectively. The amount of plastic strain decreases by over an order of magnitude from the 50 μm model to the 400 μm model as was typical throughout all the models. In general, the more detailed models experienced plastic strains in the hundreds of percents, with the less detailed, wavy surface models (400 μm) experiencing less than 20 percent plastic strain. This change in contact from mostly 'ploughing' through asperities compared to 'sliding' over asperities accounts for the major changes in the force resultants such as Figures 19-22.

The slipper part of the model experienced very little strain during the sliding simulations. Only on the finer models did any significant plastic strain occur. When plastic strains were experienced they were typically less than two percent. This was expected, since the rail was modeled as perfectly plastic with a yield strength approximately three times smaller than the static yield strength of the slipper.

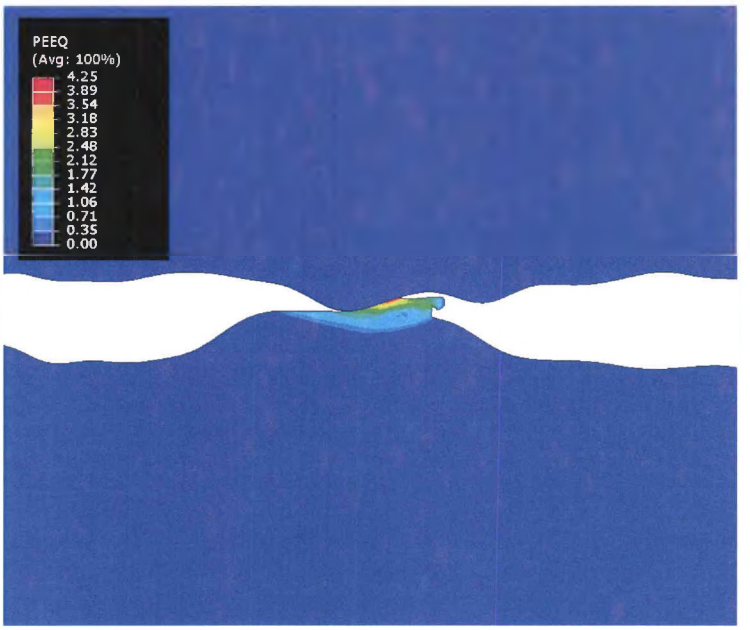

Figure 25: Asperity deformation, model 2 (50 μm filter)

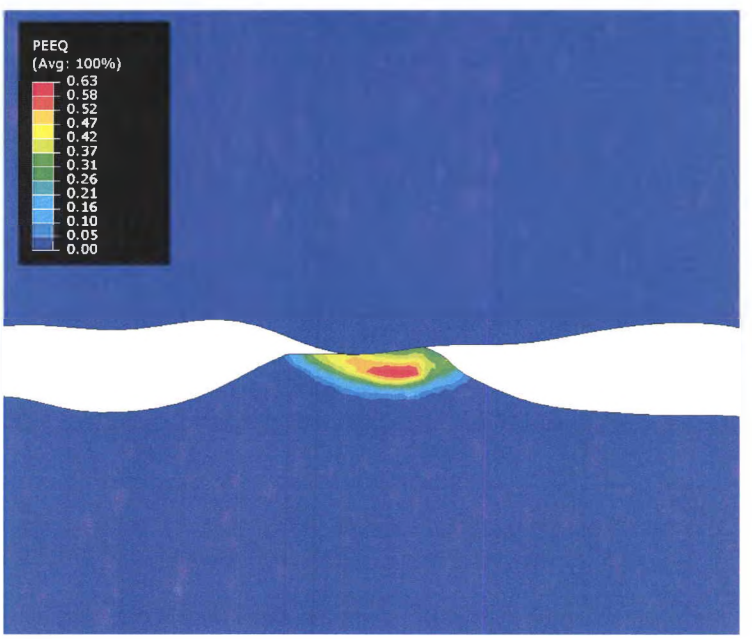

Figure 26: Asperity deformation, model 2 (100 μm filter)

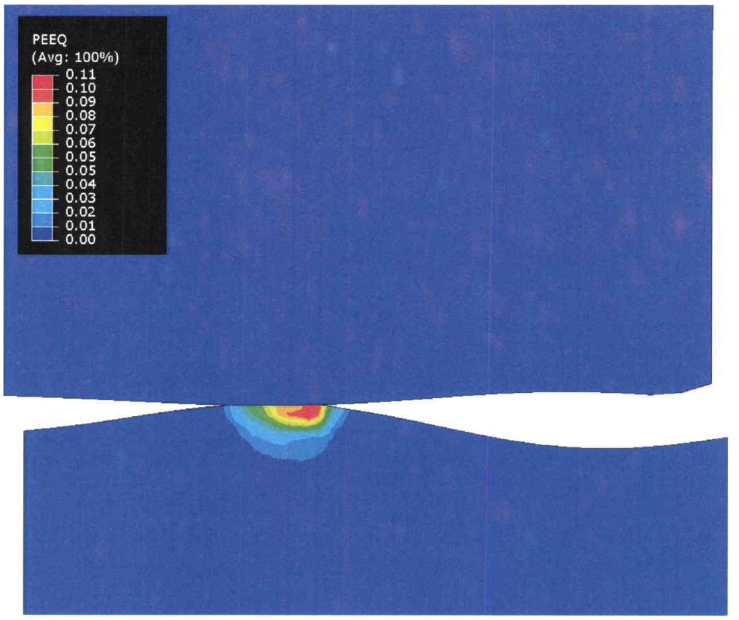

Figure 27: Asperity deformation, model 2 (400 μm filter)

Friction Dependence on Model Resolution

The first variable considered in this study was the effect of the filtering on the coefficient of friction for each of the models. To ensure continuity, all the models used a consistent pressure (8.76 Mpa), sliding velocity (.005 ft/sec), as well as model friction coefficient (0.2). The results of each of the individual models can be seen in Figure 26. Not all the simulations were able to be run to completion. The large amounts of deformation experienced in certain models created instances where the finite element mesh became excessively distorted, to the point that the simulation would automatically terminate. Data from these simulations was not included in the results. It can be seen that only the finer models had this problem, as all models filtered at 100 μm or higher successfully ran.

As expected the measured frictional coefficient tends to decrease as the filter length becomes longer, although each model contains certain specific variations. Model 1 was the only model to have all its simulations run successfully. Like the force- displacement curve in Figure 17, the frictional behavior of the 100 μm version of this model does not follow the overall trend exhibited by the other data points within the model. Model 2 shows a constant increase in friction coefficient from 400 μm through 100 μm filters, with a large jump between the 50 μm and 100 μm filters. Model 3 was unable to run the unfiltered case and the 50 μm case. The cases that did run, however, mirrored the results from model 1 in their behavior. Model 4 had the overall lowest frictional coefficients at all filter wavelengths.

It can also be seen that as the models were filtered their frictional coefficients became less scattered. At the 200 μm filter, all except model 4 show very similar

results and at 400 μm the frictional coefficients are very nearly the same. It is also of note that for the 400 μm model the measured coefficient of friction is within 10 percent of the model friction coefficient which was set at 0.2 for these simulations. Therefore, it could be said that at this point the geometry has almost completely stopped contributing to the frictional forces, with only the surface interaction properties describing the friction. The waviness of the surfaces has become negligible, and a purely flat surface can be considered.

Figure 27 combines the data from all the models and adds a second order fit. It can be seen that the curve puts the unfiltered case at a friction coefficient of 0.49, with 0.29 of this being attributed to the geometry and 0.2 being attributed to the prescribed surface interaction.

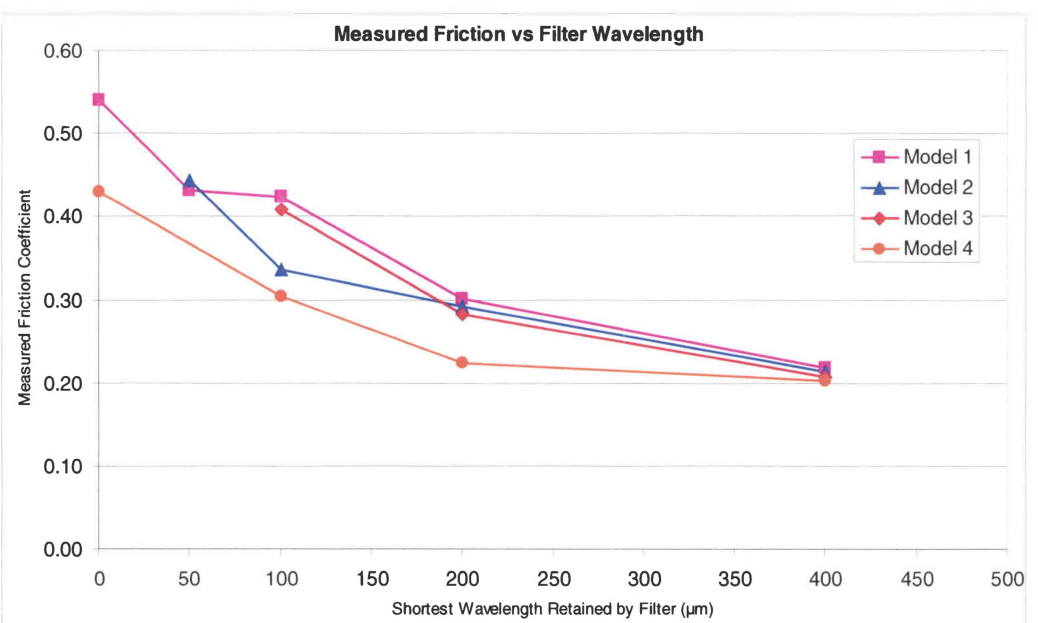

Figure 28: Analysis of friction coefficient for individual models

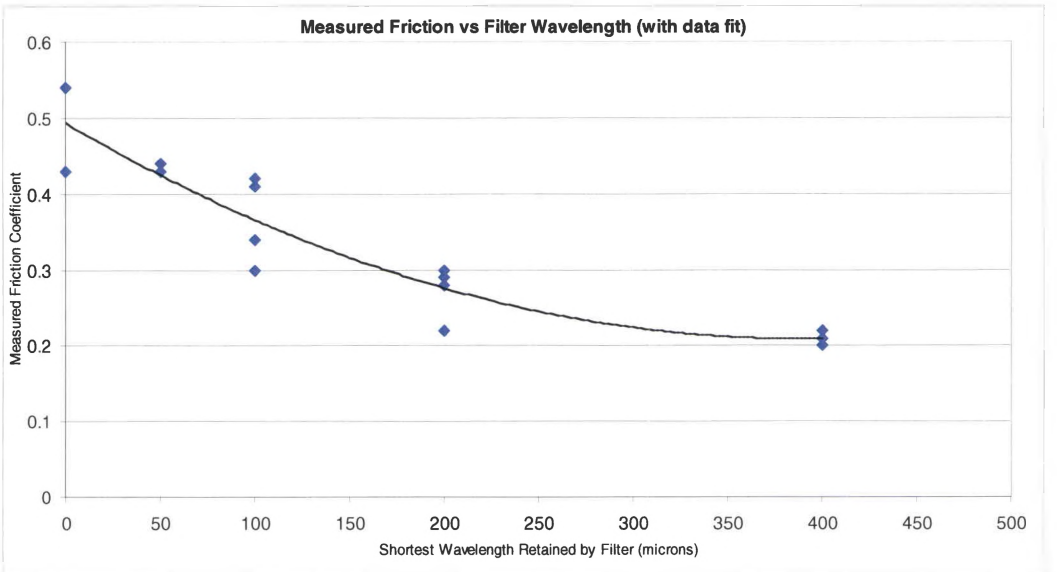

Figure 29: Analysis of friction coefficient with second order data fit

Another variable studied within this report was the effect of the prescribed model friction on the measured friction. While kept at a constant value of 0.2 for the multiple model simulations, the effect of using this value needed to be checked. Only model 1 was used in this study, with the 50 μm and 100 μm filtered versions representing the more detailed models and the 400 μm and 600 μm models representing the flatter or less detailed models. Figure 28 shows the results of the simulations. Each of the models displays a mostly linear relationship, with a slight variation occurring for the 100 μm model. The slope of the more filtered models is very near 1, with the more detailed models showing a slightly higher slope at approximately 1.25.

Figure 29 shows the normalized or effective values of friction vs. prescribed model friction. Here, a clear distinction in behavior can be seen between the different

types of models. The more detailed models show a highly non-linear relationship which very closely follows a power law fit in Eq. 11, where μ_{eff} is the measured friction coefficient divided by the prescribed model friction coefficient (μ_0). The less detailed models show no effect from the different friction parameters, however.

$$\mu_{eff} = 0.897\mu_0^{1.56} \tag{11}$$

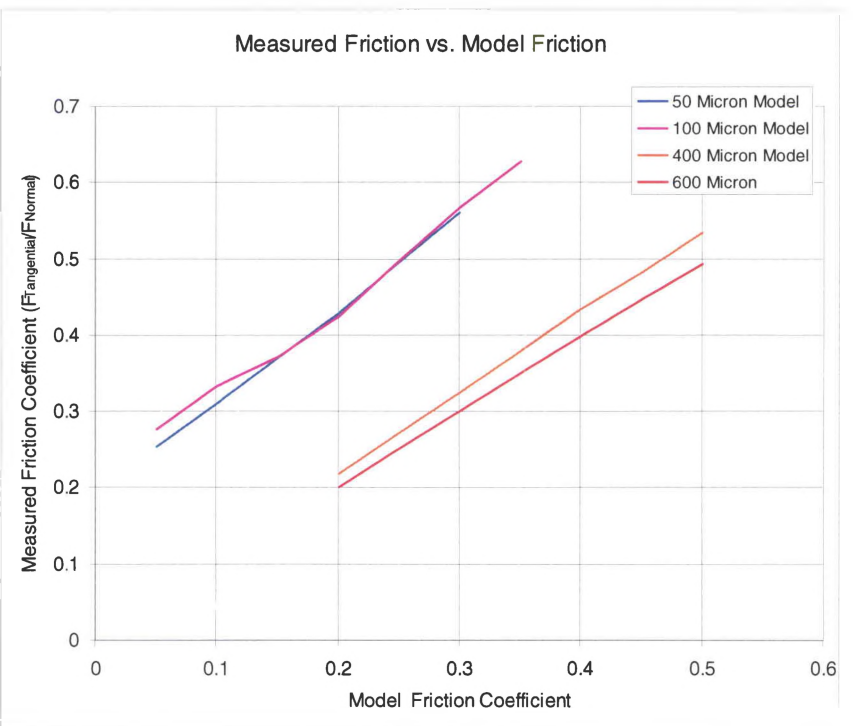

Figure 30: Effect of prescribed model friction on measured friction at various filters

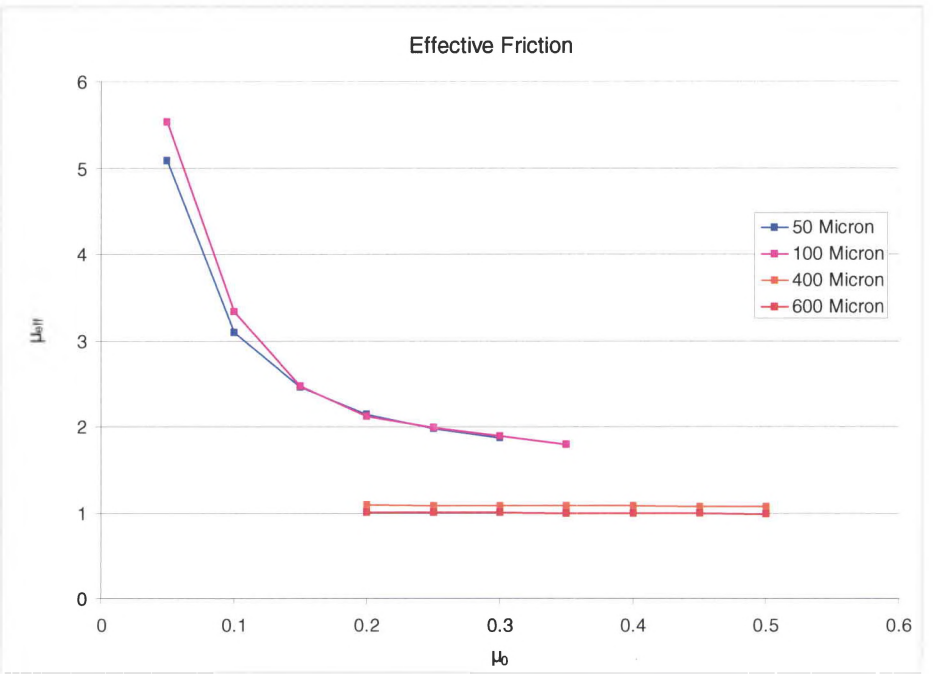

Figure 31: Effective friction at various filters

Friction Dependence on Pressure & Velocity

In order to gain a better understanding of relationship between pressure, velocity and friction a selected number of models were used to check what effect altering these variables had on the measured friction coefficient. Model 1 was again used for the pressure variation portion of the study, with the 100 μm and 400 μm models representing the 'rough' and 'flat' scenarios. Figure 30 shows the results of changing pressure on these particular models. As before, a constant model friction coefficient (0.2) was used along with a constant velocity (0.005 ft/s). The finer model displays a much higher overall friction coefficient, as well as a much more variable one as compared to the flatter 400 μm model. Like before, very little effect is seen on

this model with respect to pressure, with the friction coefficient hovering right above the prescribed value of 0.2.

The 100 μm model shows a decrease in friction with pressure up until the 26 MPa simulation. The result at that pressure is questionable, however, since incredibly large deformation occurred. In fact, so much deformation took place that only a very small section of rail was able to be traversed before ABAQUS would terminate the simulation due to excessive strains. Also, a finer mesh was required compared to the other simulations, which could have affected the results negatively. Because of this, the 26 MPa simulation was not considered further.

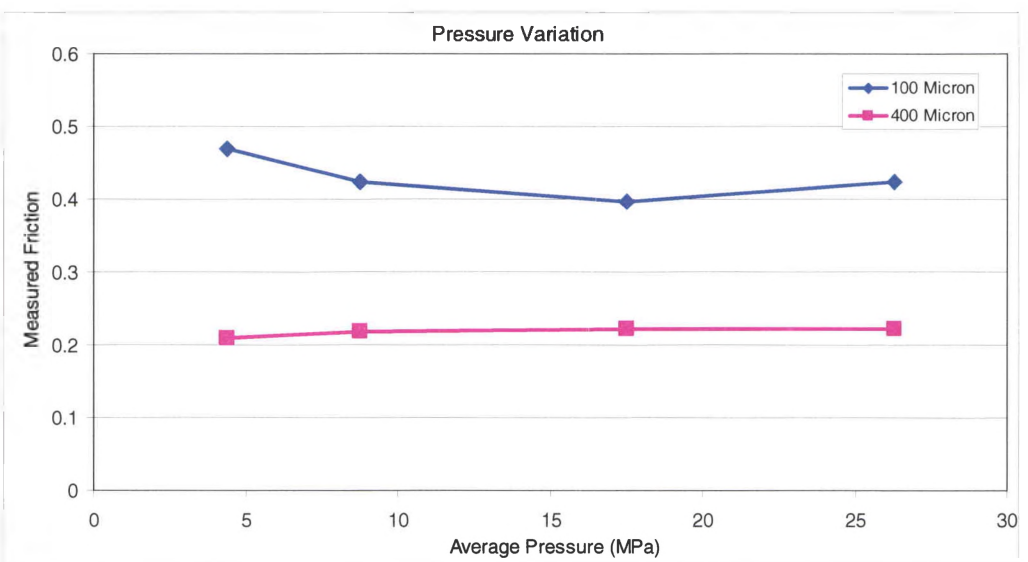

Figure 32: Measured friction with pressure variation

Previously, Cameron and Palazotto [23], using data from Montgomery [24], developed a relationship for a dynamic friction coefficient dependent upon pressure (P) and velocity (v) seen in Eq. 12. The exponent (n) was found to be -0.2299 through use of empirical measurements. The form in Eq. 13 was used to derive the exponent (n) for the data in the current study. Table 5 show the values used to plug into Eq. 14 to solve for the variable, as well as the value of n itself. As can be seen, a large difference occurs between the exponent found in [23] and those derived herein. Also, some variation in n is seen within this study, with values ranging from -0.0949 to -0.1455.

$$\mu = (Pv)^n \tag{12}$$

$$(\mu_1 / \mu_2) = (P_1 / P_2)^n \tag{13}$$

$$n = \log_{(P_1 / P_2)}(\mu_1 / \mu_2) \tag{14}$$

Pressure	μ
(P_1) 4.38	0.469
(P_2) 8.76	0.424
(P_3) 17.51	0.397

Ratio	(P) Ratio	(μ) Ratio	n
P_2/P_1	2	0.9041	-0.1455
P_3/P_2	2	0.9363	-0.0949
P_3/P_1	4	0.8465	-0.1202

Table 5: Pressure and friction parameters and derived exponent (n)

To further explore the effects of pressure change, the Model 1 100 μm model was used in altering both model friction coefficient and pressure simultaneously. The results can be seen in Figure 31. The drop in friction coefficient can be seen with increase in pressure at all values of prescribed model friction coefficient, although the difference in the two changes slightly. Using the same technique as above, a value for the exponent (n) in Eq.'s 3 and 4 is again derived. Table 6 shows the values used as well as the results for n. The value for n increases with an increase in model friction, going from -0.1245 to -0.0866. The mean value for n was -0.1038, which is slightly larger than the average of -0.1202 derived earlier, but still relatively close compared to the -0.2299 reported in [23].

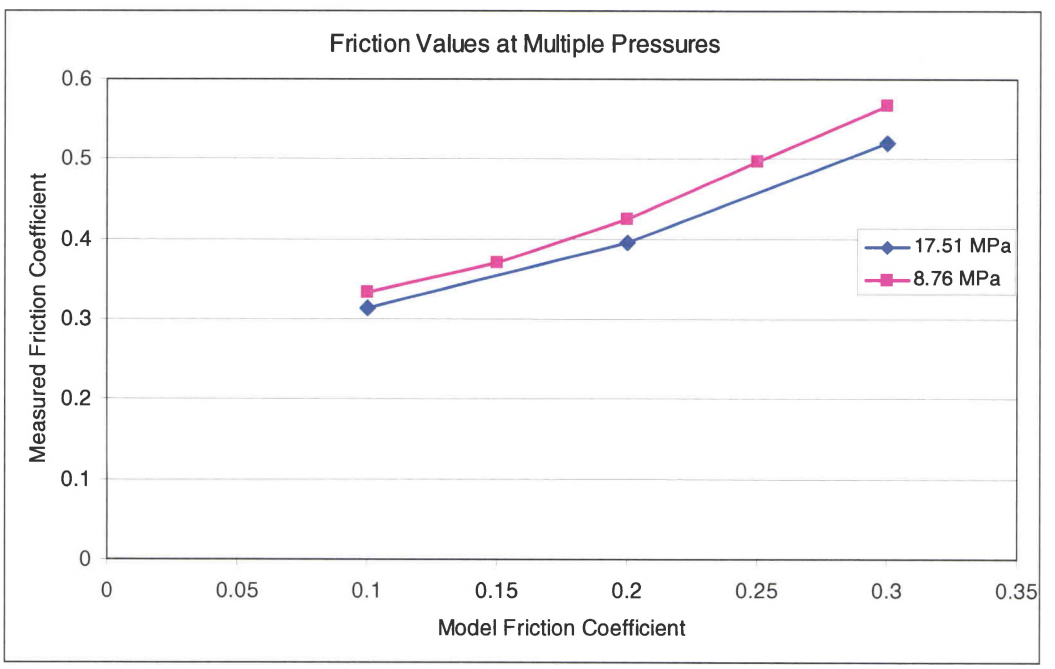

Figure 33: Friction coefficient with variable pressure and model friction

	$\mu_0 = .1$	$\mu_0 = .2$	$\mu_0 = .3$
$\mu_{measured}$ (8.76 MPa)	0.333	0.4242	0.5671
$\mu_{measured}$ (17.51 MPa)	0.3136	0.3957	0.5202
Ratio	0.917	0.933	0.942

μ_0	(P) Ratio	(μ) Ratio	n
0.1	2	0.917	-0.1245
0.2	2	0.933	-0.1003
0.3	2	0.942	-0.0866

Table 6: Pressure and friction parameters and derived exponent (n) at varying levels of prescribed model friction (μ_0)

In keeping with the model for friction described in [23], the effect of changing the velocity variable was studied as well. Two different models were used in this study, models 1 and 2, both filtered at the 100 μm level. The constant pressure of 8.76 MPa was used, along with a model friction of 0.2 as before. The results can be seen in Figure 32. The models have an overall difference in friction coefficient, as expected from Figure 26. However, the behavior appears different, with a jump in friction at the lower sliding speeds for Model 1 and at the higher speeds for Model 2. Besides these jumps, very little effect is seen on varying the sliding velocity, with only a slight decrease in friction with increase in velocity.

Unlike the pressure change study, altering the velocity does not follow a regular pattern for either of the models. Also, while the results for the most part show little variation, the force resultants reveal a source of error involved with the velocity change study. Figures 33 and 34 show the force resultants for Model 2 at 0.06 in/sec

and 0.24 in/sec. A nine point moving average was included to filter out the high frequency noise. A clear increase in both wavelength and amplitude can be seen for the 0.24 in/sec simulation as compared to the slower 0.06 in/sec simulation. While the forces still fluctuates around 0, this occurrence could alter the averages of the forces which were used to calculate the overall frictional forces.

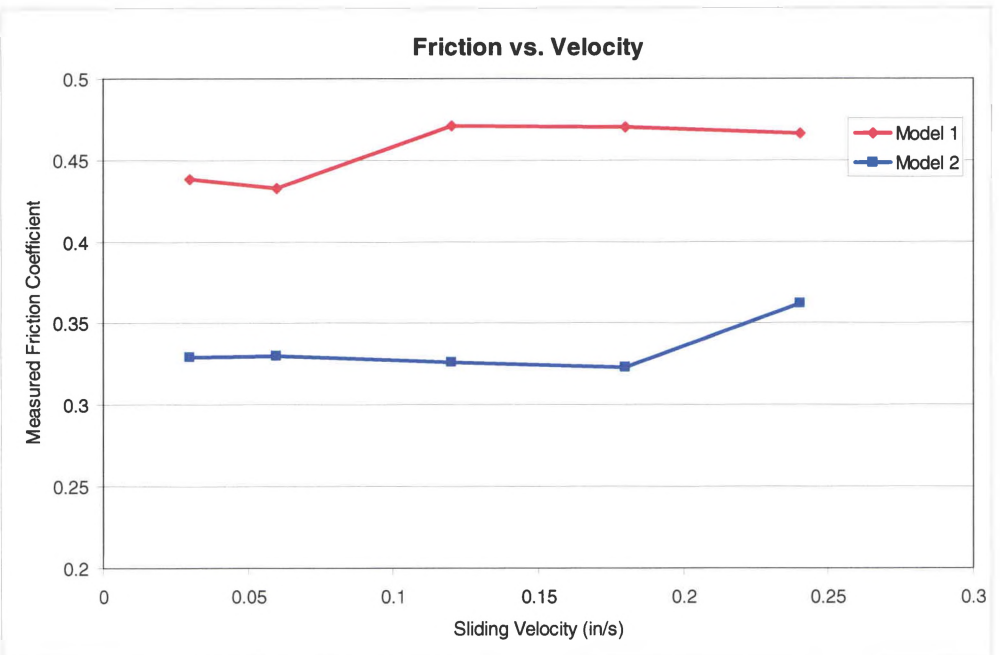

Figure 34: Measured friction with velocity variation

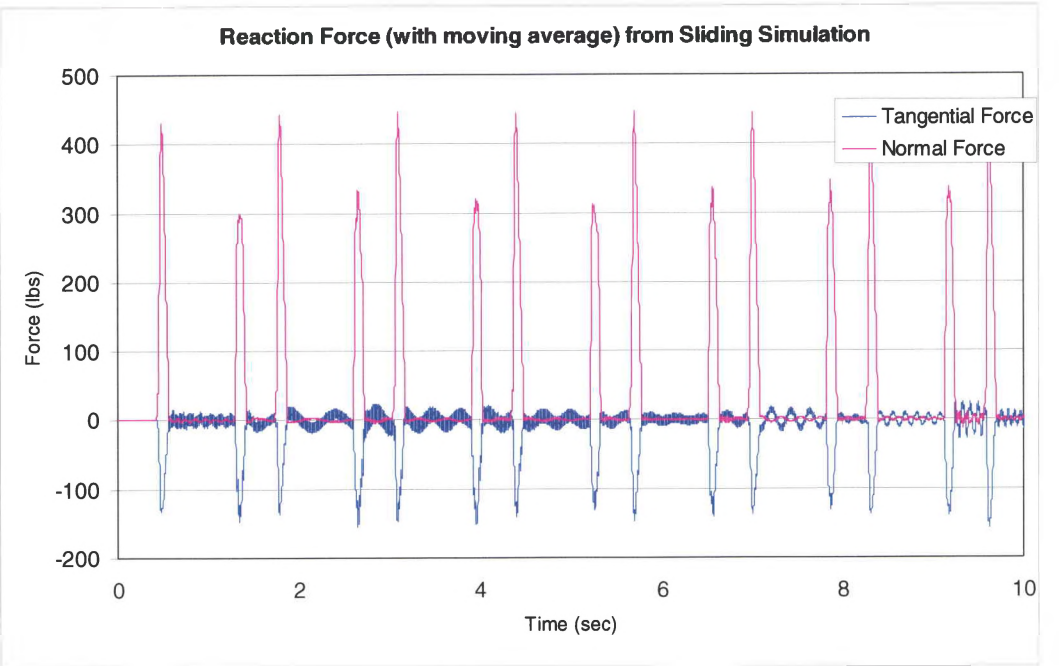

Figure 35: Force resultant from model 2 (100 μm) sliding simulation

(v = 0.06 in/sec)

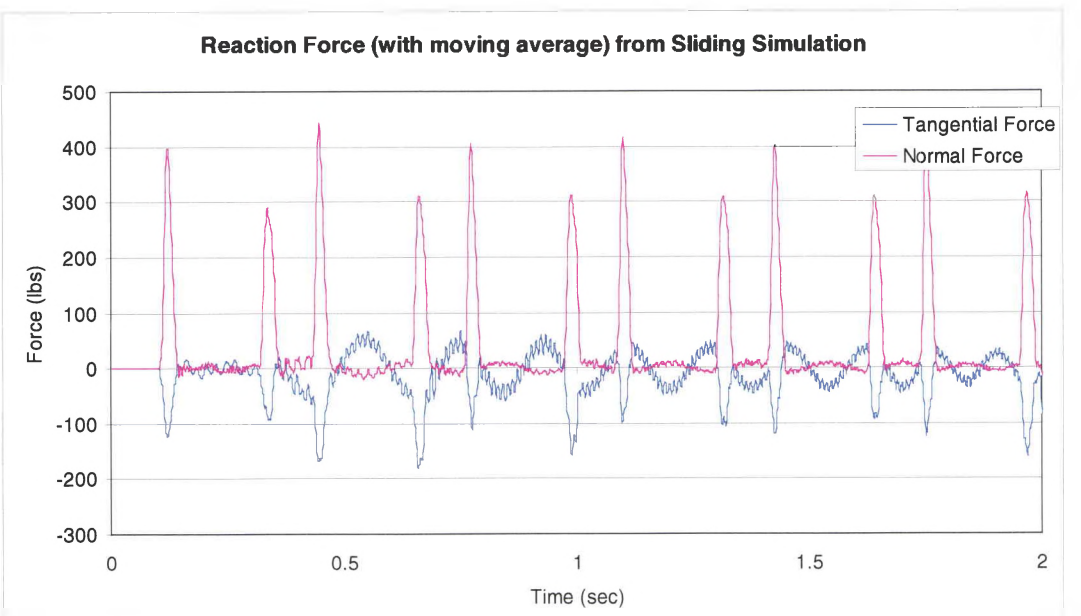

Figure 36: Force resultant from model 2 (100 μm) sliding simulation

(v = 0.24 in/sec)

CHAPTER VI

CONCLUSIONS

Finite element models have been constructed to investigate the dependence of the coefficient of friction upon model characteristics as well as physical variables. Detailed, three-dimensional surface roughness measurements were taken from unused rail, slipper, and slipper insert samples from Holloman High Speed Test Track (HHSTT). The surfaces were characterized according to commonly used statistical measures and converted into two-dimensional surfaces, which were then filtered using a low-pass spatial filter at varying wavelengths to represent varying levels of surface roughness and waviness. Plane strain finite element models were created using the filtered surface profiles in order to simulate the sliding event experienced at HHSTT, with tangential and normal reaction forces describing effective friction coefficient.

Relationships were established between this friction coefficient, surface topography, and specified friction interaction contained in the model definitions. When keeping the specified friction interaction constant, a clear decrease in effective friction coefficient was seen with increasing the filter wavelength, roughly following a second order trend. Also, the type of asperity deformation transitioned from a

mostly plastic 'ploughing' regime in the detailed models to a more elastic 'sliding' regime in the wavy or less detailed models. The specified model friction interaction itself produced a large variation in effective friction for the rougher, more detailed models, approximately following a power law formulation. The wavier models showed little to no effect from altering the model friction definitions, with the measured and model friction values being essentially equal.

The physical parameters of contact pressure and sliding velocity were also studied on a limited number of models. Altering the pressure produced results which follow the same power law pattern described in [23], with derived exponents being highly variable, yet overall smaller in absolute value than those found in [23]. The sliding velocity study did not yield results following this same pattern, and were not of much significance due to the high amplitude and wavelength noise found in the force resultant data as velocities increased.

Recommendations for future work include using thermomechanical coupling in order to introduce the effects of the heat generated by the frictional sliding. Also, determining how to increase model sliding velocity, while accurately accounting for inertial effects would be useful, along with the inclusion of a failure model to represent erosion due to wear. Finally, including more model data by using larger surface profiles is recommended, as fewer isolated surface features would heavily impact the overall analysis.

BIBLIOGRAPHY

1. Bowden, F. P., and Tabor, D., *The Friction and Lubrication of Solids*, Clarendon Press, Oxford, 1950.

2. Bowden, F.P., and Leben, L., The nature of sliding and the analysis of friction, *Proc. of the Roy. Soc. of London. Series A*, Vol. 169, 1939, pp. 371-391.

3. Bowden, F.P., and Tabor, D., The area of contact between stationary and between moving surfaces, *Proc. Of the Roy. Soc. of London, Series A*, Vol. 169, 1939, pp. 391-413.

4. Archard, J.F., Contact and rubbing of flat surfaces, *Journal of Applied Physics*, Vol. 24, 1953, pp. 981-988.

5. Green, A.P., Friction between unlubricated metals: a theoretical analysis of the junction model, *Proc. of the Roy. Soc. of London, Series A*, Vol. 228, 1955, pp. 191-204.

6. Archard, J.F., Elastic deformation and the laws of friction, *Proc. of the Roy. Soc. of London, Series A*, Vol. 243, 1957, pp. 190-205.

7. Greenwood, J.A., and Williamson, J.P.B., Contact of nominally flat surfaces, *Proc. of the Roy. Soc. of London, Series A*, Vol. 295, 1966, pp. 300-319.

8. Whitehouse, D.J., and Archard, J.F., The properties of random surfaces of significance in their contact, *Proc. of the Roy. Soc. of London, Series A*, Vol. 316, 1970, pp. 97-121.

9. Onions, R.A., and Archard, J.F., The contact of surfaces having a random structure, *J. Phys. D: Appl. Phys.*, Vol. 6, 1973, pp. 289-304.

10. Ogilvy, J.A., Numerical simulation of friction between contacting rough surfaces, *J. Phys. D: Appl. Phys.*, Vol. 24, 1991, pp. 2089-2109.

11. Ogilvy, Numerical simulation of elastic-plastic contact between anisotropic rough surfaces, *J. Phys. D: Appl. Phys.*, Vol. 25, 1992, pp. 1789-1809.

12. Ford, I.J., Roughness effect on friction for multi-asperity contact between surfaces, *J. Phys. D: Appl. Phys.*, Vol. 26, 1993, pp. 2219-2225.

13. Tabor, D. *The Properties of Diamond* (ed. J. E. Field), ch. 10, London: Academic Press.

14. Tangena, A.G. and Wijnhoven, P.J.M., Finite element calculations on the influence of surface roughness on friction, *Wear*, Vol. 103, 1985, pp. 345-354.

15. Faulkner, A. and Arnell, R.D., The development of a finite element model to simulate the sliding interaction between two, three-dimensional, elastoplastic, hemispherical asperities, *Wear*, Vol. 242, 2000, pp. 114-122.

16. Franse, J., Tangena, A.G., and Wijnhoven, P.J.M., The influence of asperity deformation and surface roughness on the coefficient of friction during sliding, in: D. Dowson, C.M. Taylor, M. Godet, D. Berthe_Eds.., Proc. 12th Leeds–Lyon Symp. On Tribology, Lyon, September 1985, Butterworths, London, 1986.

17. Vijaywargiya, R. and Green, I., A finite element study of the deformations, forces, stressformations, and energy losses in sliding cylindrical contacts, *Int. J. of Non-Linear Mechanics*, Vol. 42, 2007, pp. 914-927.

18. Torrace, A.A., Galligan, J. and Liraut, G., A model of the friction of a smooth hard surface sliding over a softer one, *Wear*, Vol. 212, 1997, pp. 213-220.

19. Dick, T. and Cailletaud, G., Analytic and FE based estimation of the coefficient of friction of composites surfaces, *Wear*, Vol. 260, 2006, pp. 1305-1316.

20. Wyko NT800 Optical Profiling Systems, Veeco Instruments Inc., Tucson, Arizona, 2002.

21. ABAQUS Analysis User's Manual, Version 6.8, Dassault Systems Simulia Corp., Providence, Rhode Island, 2008.

22. Cinnamon, J.D., Palazotto, A.N., and Kennan, Z., Material Characterization and Development of a Constitutive Relationship for Hypervelocity Impact of 1080 Steel and Vascomax 300, *Int. J. Impact Eng.*, Vol. 33, 2006, pp. 180-189.

23. Cameron, G., and Palazotto, A.N., An Evaluation of High Velocity Wear, *Wear*, Vol. 265, 2008, pp. 10066-1075.

24. Montgomery, R.S., Friction and Wear at High Sliding Speeds, *Wear*, Vol. 36, 1976, pp. 275-298.